Materials Today Bio 32 (2025) 101694

Contents lists available at ScienceDirect

Materials Today Bio

journal homepage: www.journals.elsevier.com/materials-today-bio

Immune cell targeting-mediated cytomimetic drug delivery system for BBB-penetrating and precise therapy of in situ glioma

Xiu Wang [a,b], Baoqin Song [a], Mengru Wu [a], Lijing Qin [a], Wanjun Liang [a,b,c,*]

[a] School of Pharmaceutical Sciences & Institute of Materia Medica, Shandong First Medical University & Shandong Academy of Medical Sciences, China
[b] State Laboratory of Advanced Drug Delivery and Control Release System, Shandong First Medical University, China
[c] Key Laboratory for Biotechnology Drugs of National Health Commission, Shandong Academy of Medical Sciences, China

ARTICLE INFO

Keywords:
Cytomimetic drug delivery system
Blood brain barrier penetration
Visualization
Endogenous controlled drug release
Orthotopic glioma therapy

ABSTRACT

Gliomas are a group of highly malignant tumors that are prone to recurrence after surgery. Due to the limitation of the blood-brain barrier (BBB), most antitumor drugs cannot cross it. Therefore, improving the delivery efficiency of antitumor drugs in their treatment remains a significant challenge. Herein, we report a unique cellular biomimetic drug delivery system (CTP@RAW) that benefits from the exceptional immune homing and long-term tracking ability of RAW 264.7 cells to specifically penetrate BBB and target tumor sites. The drug (TMZ) is encapsulated in RAW264.7 to avoid being cleared or degraded by the blood, improve bioavailability and reduce systemic toxicity. And that, owning to polydopamine (PDA) coating on the quantum dots-drug nanoparticles, which can endogenously and controllably release TMZ in response to certain tumor microenvironment (high GSH and low pH). This delivery system can also achieve precise localization and real-time visualization of tumors via fluorescence imaging. The released drugs effectively inhibit tumor growth by regulating cytokine expression levels, including GFAP, Ki67, Caspase-3, and TNF-α. Our study demonstrates that this drug delivery system can cross BBB, improve drug delivery efficiency, and has excellent potential for visualization and precision treatment of in situ gliomas.

1. Introduction

Gliomas are a group of primary cranial malignant tumors with a high incidence and low curative rate, which can seriously endanger human health [1,2]. Due to tumor heterogeneity and aggressiveness, as well as physiological barriers, these gliomas are often difficult to identify accurately, and their diagnosis, monitoring, and treatment are challenging [3–5]. Therefore, achieving the precise targeted delivery of therapeutic drugs is a significant challenge in this field [6]. The highly selective nature of the blood-brain barrier (BBB) prevents most diagnostic drugs from entering the tumor region, leading to inaccurate diagnosis and poor therapeutic outcomes [7–9]. It has been reported that less than 5 % of the molecules tested in the field of drug discovery for this disease can cross the BBB, and a small number of these drugs still struggle to reach the concentrations required for treatment once they enter the cranium [10,11]. Researchers have been trying to enhance drug-delivery efficiency with nano-drug delivery vehicles like extracellular vesicles, liposomes, hydrogels, micelles, polymers, inorganic NPs [12]. However, most of these vehicles need more specific selectivity for the brain and tend to be enriched in organs such as the liver and spleen, making them difficult to be effective [13–15]. Materials with adaptive deformation capacities have also been discovered to further amplify the interaction between drug particles and cells [16]. Recently, Fan group have developed fruit-derived extracellular vesicles as drug carriers loaded with drugs, enabling them to cross BBB by receptor-mediated endocytosis and membrane fusion, achieving efffcient therapy of glioma [17–19]. The latest research shows that cell-mediated biomimetic drug delivery systems can exhibit excellent performance, which has attracted the wide attention of researchers [20–23]. The report claims that the cell-mediated active targeted drug delivery system can penetrate the BBB while selectively accumulating in the tumor region, which can better enhance the drug's therapeutic activity in vivo, achieve precise targeted delivery, and reduce the adverse effects of the drug [24,25]. Typical examples are immune cells, which can naturally cross the BBB and be identified and recruited to the site of the lesion [26–28]. Among them, macrophages, as a natural immune cells and antigen

* Corresponding author. School of Pharmaceutical Sciences & Institute of Materia Medica, Shandong First Medical University & Shandong Academy of Medical Sciences, China.
E-mail address: liangwanjun@sdfmu.edu.cn (W. Liang).

https://doi.org/10.1016/j.mtbio.2025.101694
Received 29 January 2025; Received in revised form 7 March 2025; Accepted 20 March 2025
Available online 22 March 2025

presenting cells, have the natural ability to phagocytic nanoparticles and a long blood half-life, which can overcome the metabolic problems of drugs during transportation [29,30]. Therefore, the use of macrophages for chemical drug delivery leads to a significant increase in drug accumulation in gliomas, which provides an important carrier support for the establishment of cell-simulated drug delivery systems for accurate diagnosis and treatment [31,32]. This further provides a feasible basis for developing novel drug delivery research in real-time visualization and precise treatment of gliomas.

In brain glioma visualization, another challenge is ensuring that the probe delivered to the tumor site can output a sensitive signal [33]. Currently, optical bioimaging, as a powerful technique for monitoring the biological behavior of living systems, has the advantages of visualization, immediacy, and high sensitivity, which have made it indispensable in life science research [34–36]. In particular, representative semiconductor quantum dot probes have unique advantages over other probes, such as narrow emission peaks, outstanding optical stability, and a wide range of excitation wavelengths [37,38]. Among them, the recent emergence of new I-III-VI $CuInS_2$ quantum dots, which do not contain toxic class A elements (Cd, Pb, Hg) or class B elements (Se, As), has just solved the problem of biotoxicity of traditional quantum dots and facilitated the development of fluorescent probes for visualization of drug delivery and in vivo imaging [39,40].

Designing controlled release properties for drug delivery carriers is critical to precise drug delivery, reducing toxic side effects, and improving bioavailability. Therefore, it is crucial to construct suitable controlled-release devices when designing drug delivery systems. Polydopamine (PDA) is a multifunctional material with good biocompatibility, adhesion, high chemical reactivity, and multiple drug release response mechanisms [41–43]. PDA is used to design of multiple stimulus-responsive drug release mechanisms that can respond to endogenous stimulation of specific pH and glutathione (GSH) [44–48]. This can stabilize the drug in the delivery vehicle in the blood circulation, and achieve the drug release in the tumor microenvironment [49,50]. The microenvironment can realize the drug's intelligent release, which can both reduce the drug's toxicity in the body and improve the therapeutic efficiency [51,52]. These properties present an excellent potential for its application in controlled drug release. In addition, designing an excellent drug delivery system also requires a reasonable tumor model to provide an accurate assessment basis [53,54]. In vitro, three-dimensional (3D) tumor models can better simulate the spatial structure and growth environment of in vivo tumors, retain the pathological and genetic characteristics of tumor cells, and reflect the complex interactions between tumor cells and their microenvironment. They have gradually become a powerful tool for the study of tumor mechanism, drug screening, and individualized tumor treatment [55–58].

To achieve precise delivery and real-time visualization of gliomas, we proposed to develop an immune cell targeting-mediated cytomimetic drug delivery system (CTP@RAW) based on the targeting properties, immediate tracing, and controlled release, as shown in Fig. 1. Benefit from the high signal-to-noise imaging of quantum dot materials that can be used to visualize deep brain tumor regions covered by thick skulls and the unique immune homing and the long-term tracing ability of RAW264.7 cells, CTP@RAW showed unique recognition of gliomas and drug delivery ability to across the BBB. Our research focuses on a novel drug delivery system that encapsulates temozolomide (TMZ), an anti-glioma drug, within polydopamine (PDA) on the surface layer of quantum dots (CZQDs) nanoparticles. This method not only reduces drug toxicity in vivo but also responds to the specific environmental conditions of high glutathione (GSH) concentration and low pH. The acidic tumor microenvironment, which contains significantly more glutathione than the typical physiological environment, plays a crucial role in triggering the degradation of the nanocarrier, allowing for a controlled release of temozolomide. In addition, macrophages, which have an innate homing ability for immune responses, can prolong the residence time of temozolomide in the lesion area, significantly regulate the expression levels of cytokines such as GFAP, Ki67, Caspase-3, and TNF-α in vivo, and ultimately improve the therapeutic effect of TMZ. This delivery system, with its active targeting and penetration of the BBB, high signal-to-noise ratio, real-time visualization, and integration of precision diagnosis and treatment of gliomas, is a testament to the precision of modern medical science.

2. Materials and methods

2.1. General information

Aladdin Biochemical Technology Co., Ltd. supplied dopamine and 3-

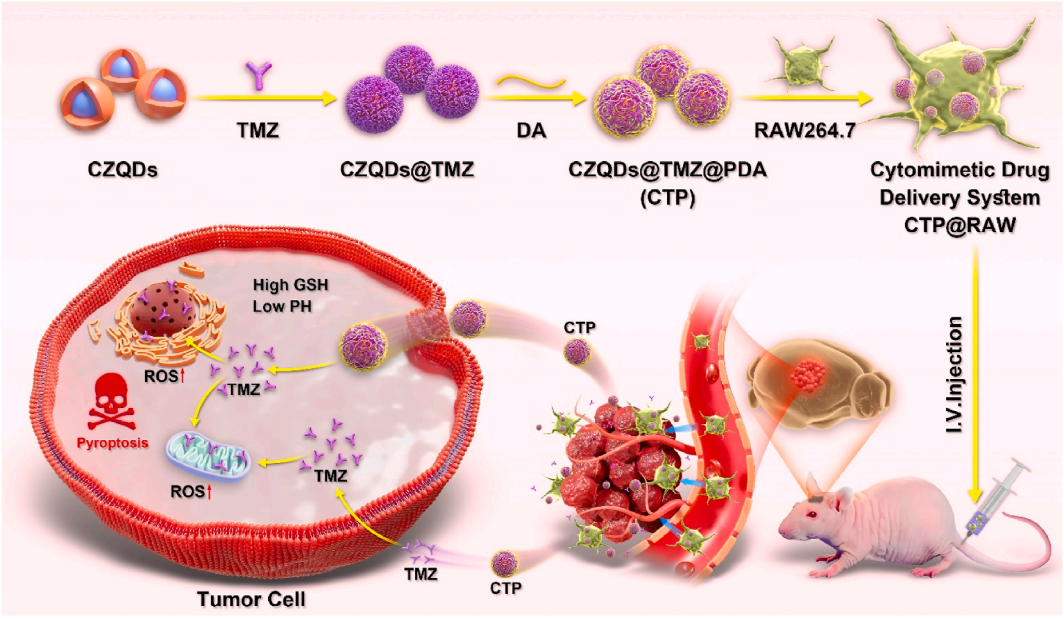

Fig. 1. The establishment schedule of an advanced cytomimetic drug delivery system that can penetrate the blood-brain barrier and target tumor sites, allowing for precise diagnosis and integrated treatment of orthotopic gliomas while significantly enhancing drug efficacy.

(4,5-dimethylthiazol-2-yl)-2,5-diphenyltetrazolium bromide (MTT). Temozolomide (TMZ) was acquired from Sigma-Aldrich. Beyotime provided us with phosphate-buffered saline (PBS). Sigma-Aldrich supplied the Calcein-AM/PI double stain kit and the ROS kit. Calcein-AM, FITC, and Hoechst33342 were acquired from Shanghai McLean Biochemical Co., LTD. Reed Biotech LTD provided mouse TNF-α, GFAP, and Caspase-3 ELISA kits. We obtained RAW264.7, U87-MG, and bEnd.3 cells from the Chinese Academy of Sciences Cell Bank. They were kept in a 1 % penicillin-streptomycin solution (Solarbio) and DMEM (Biological Industries) supplemented with 10 % fetal bovine serum (Gibco) at 37 °C with 5 % CO_2. We purchased 0.25 % trypsin digestion-EDTA from Solarbio. Every experiment was carried out using cells in the exponential growth phase. The serum and blood used in the experiment were all obtained from healthy mice. BALB/c mice were bought from Jinan Pengyue Laboratory Animal Breeding Co., LTD., which produced mice that weighed 20 g on average, or about 6 weeks old. The Shandong First Medical University School of Pharmacy and Pharmaceutical Sciences and Institute of Materia Medica's Institutional Animal Care and Use Committee's recommendations were followed when conducting the experimental animal operations (No: W202403010).

2.2. Characterizations

The nanoformulations' morphology was examined using a transmission electron microscope (HT7800, Hitachi, Japan). A Zeta-sizer Nano (ZS-90, Malvern, UK) was used to detect the size distribution. An inverted fluorescent microscope (IX83 + DP80, Olympus, Japan) was used to get cell imaging. A UV–vis spectrometer (UV2600i, Shimadzu, Japan) was used to obtain the UV–vis spectrum. A multipurpose microplate detector (Synergy H1, Biotek, USA) was used to gather the ELISA assay. The biodistribution was obtained in vivo and in vitro through a small animal imaging system (Lumina XRMS III, PerkinElmer, USA).

2.3. Preparation of $CuInS_2$/ZnS-TMZ quantum dots

Dissolve 0.034 g (0.10 M) $CuCl_2{\cdot}2H_2O$ in 20 mL deionized water and 1.106 g (1.00 M) $InCl_3$ in 5 mL anhydrous ethanol, respectively. 5.882 g (1.00 M) sodium citrate was dissolved in deionized water (20 mL), and 6.02 g (2.50 M) $Na_2S{\cdot}9H_2O$ was dissolved in 20 mL deionized water. In a three-neck flask, $CuCl_2$ solution 0.5 mL, $InCl_3$ solution 0.05 mL, sodium citrate solution 0.8 mL, glutathione 0.0305 g, and deionized water 40 mL were added successively. Under magnetic stirring, a Na_2S solution of 0.124 mL was added rapidly. The $CuInS_2$ QDs were obtained by reflux reaction at 95 °C, and the Cu:In ratio was 1:1, then dispersed in water (5 mL) at 4 °C.

0.176 g (0.04 M) $Zn(OAc)_2{\cdot}2H_2O$, 0.061 g thiourea, and 0.368 g glutathione were dissolved together in 20 mL deionized water, and the pH of the solution was adjusted to 8–9 with 1.0 M NaOH solution as the Zn precursor solution. 1.35 mL of the Zn precursor solution was added into the prepared $CuInS_2$ solution, and the $CuInS_2$/ZnS quantum dots solution was obtained by constant temperature reflux reaction at 95 °C. Finally, the prepared $CuInS_2$/ZnS quantum dots (CZQDs) were dispersed in deionized water and then stored at 4 °C.

After 5 min of ultrasonography, 1 mL of the produced CZQDs solution was added, and it was mixed for 5 h with TMZ (1.0 mL, 1.0 mg mL^{-1} in PBS). After gradient centrifugation, CZQDs-TMZ (CT) nanoparticles were the result. Lastly, 1 mL of deionized water was used to disperse the produced CT, which was then kept at 4 °C.

2.4. Preparation of CT@PDA nanoparticles

The generated ANP solution was sonicated in 1 ml of Tris-HCl buffer solution with a pH of 8.5 for 5 min. The liquid was then swirled constantly for 4 h while 5 mg of dopamine were added. The CT@PDA (CTP) nanoparticles were then distributed in 1 ml PBS and kept at 4 °C following gradient centrifugation.

2.5. Drug loading rate of CTP

CTP was initially combined with TMZ solutions at varying concentrations (in PBS with pH values of 6.8, 7.4, 8.0, and 8.5) and agitated at room temperature for 5 h. The unloaded TMZ was separated by centrifugation and washed by PBS. The concentration of TMZ in the supernatant was determined by measuring its absorbance at 330 nm in the UV–visible spectrum. We further investigated the impact of TMZ concentration (1, 5, 10, 20, 50, and 100 μg mL^{-1}) on the loading rate of CTP because it was found to be significant in deciding the loading rate. We also investigated the relationship between drug loading ratio and reaction time (10, 20, 30, 40, 50, 60 min). Drug loading rate (%) = $(c_0V_0\text{-}cV)/c_0V_0$, where c_0 (mg·mL^{-1}) and V_0 (mL) represented the initial addition concentration, and volume of TMZ, c (mg·mL^{-1}) and V (mL) represented the free TMZ's concentration and the supernatant volume.

2.6. Stability study

Storage stability: CTP was stored at 4 °C with different time points to test its storage stability. To assess the system's stability, we also did measurements of surface potential changes and the particle size at predetermined intervals of time (0, 2, 4, 6, 8, and 10 days).

Medium stability: CTP was stored at 4 °C in different medium (PBS, serum, and blood) to study the fluorescence properties.

2.7. Drug release in vitro

The drug release properties of CTP was assessed with dialysis techniques. In summary, 200 mL PBS (pH 5.0, 6.0, and 7.4) was added to a sealed dialysis bag (MW = 500, USA) containing 1 mL CTP solution. The bag was then stirred magnetically at room temperature. The dissolving media were collected at various time points (0.5, 1, 2, 4, 8, 12, 16, 20, and 24 h) and with varying pH (7.4, 6.0, and 5.0), and all test samples were shielded from light. To measure the amount of released TMZ using a UV–vis spectrophotometer, 3 mL of the PBS dissolving media was removed at each time point and replaced with 3 mL of new PBS. The effects of redox features on GSH-triggered drug release were examined under identical conditions, except for glutathione (GSH) concentration. After being transferred to a dialysis bag, 1 mL of the 0.2 mg mL^{-1} CTP solution was soaked in 100 mL of PBS, including GSH (2, 5, and 10 mM). The detection procedures and additional experimental stages described above are used here.

2.8. The preparation of the cell bionic drug delivery system CTP@RAW

RAW264.7 cells were incubated with CTP (100 μg mL^{-1}) for 3 h. Trypsin was used to break down the cells, DMEM was used to end the process, and the cells were centrifuged to produce the cell bionic drug delivery system (CTP@RAW), which was then distributed in PBS solution for future use. The cells were meticulously cleaned five times in a PBS solution after the cell growth medium was removed in order to get rid of any remaining nanoparticles.

2.9. Cytotoxicity assay

RAW264.7 cells or U87-MG cells were planted in 6-well cell culture trays. Different amounts of CTP, CT, CZQDs, or TMZ (50 μg mL^{-1}) were added to the culture system, and this mixture was then incubated for 48 h at 37 °C. 150 mL of working solution—which included 5 mL Calcein-AM solution (2 mM), 15 mL PI solution (1.5 mM), and 5 mL of buffer solution-were used to dye RAW cells. The combination was then incubated for 15 min at 37 °C. Finally, the distinction between living and dead cells - green and red fluorescence, respectively—was made using fluorescent microscopy.

Using an MTT assay, the cytotoxicity of CTP, CT, CZQDs, and TMZ was further assessed. Briefly, RAW264.7 cells were sown in culture plates (1×10^4 cells per well) and left to react for 48 h with varying concentrations of CTP, CT, CZQDs, or TMZ. After thoroughly cleaning the cells with PBS, they were placed in 100 μL of DMEM (0.5 mg mL^{-1} MTT) and incubated for 4 h. After the supernatant was removed entirely, 100 μL of DMSO was added to each well of the mixture. After gently shaking the 96-well plate for 10 min to dissolve the formaldehyde crystals, the absorbance at 490 nm was measured on a microplate reader (the background absorbance was 690 nm).

2.10. Cellular uptake of CTP

Cell imaging: RAW264.7 cells (or U87-MG cells) were inoculated in cell culture plates and incubated with CTP, CT, and CZQDs for 0.5 h, 1 h, and 4 h, respectively. Then, the medium was removed and cleaned with PBS three times, and 500 μL PBS was added to each well to observe the imaging performance of nanotherapeutic drugs in cell carriers by an inverted fluorescence microscope.

Overnight, 200 μL CTP (100 μg mL^{-1}, without FBS) was applied to incubate RAW264.7 cells that had been injected in 6-well plates. Every 30 min during the next 6 h, the fluorescence spectra of cell supernatants were examined. The loading kinetics of CTP in the cells were ascertained by comparing the spectra with those of a CTP solution (100 μg mL^{-1}). The CTP fluorescence signal was seen using a fluorescent microscope. Three measurements (n = 3) were taken concurrently.

CTP retention rate in RAW264.7 cells: Following seeding in cell culture plates, RAW264.7 cells were exposed to 200 μL CTP (100 μg mL^{-1}) for 3 h. The intensity of the CTP fluorescent spectra that the cells had ingested was used As a starting point. Before the cells were grown in fresh DMEM, they were thoroughly washed with PBS. For the following 48 h, the fluorescence intensities of the cell supernatant were monitored every 4 h. The CTP's retention ratio in RAW264.7 cells was calculated using the relationship between the intensity of CTP's cell supernatant fluorescence and its initial value. For each experiment, three measurements were made in parallel (n = 3).

2.11. Analysis of intracellular ROS level

U87-MG cells were seeded with a density of 5×10^4 cells/well in 96-well plates for quantitative investigation to detect ROS generation. Following a 24-h growth period, the cells were treated with 100 μg mL^{-1} of CTP, CT, CZQDs, or TMZ and incubated for 6 h. As a control group, cells with no material addition were used. Following incubation, 10 μM of H_2-DCFDA was added, the cells were then cultured with fresh medium, and the mixture was incubated for 30 min at 37 °C. After removing any extra H_2-DCFDA from the cells, they were cleaned with PBS and given a new medium. Utilizing a fluorescent microscope, the cells were examined for microscopic qualitative imaging. For quantitative measurements, the fluorescence intensity was measured with a microplate reader.

2.12. Drug release of CTP@RAW in vitro

In vitro *cumulative release* of CTP@RAW in DMEM (pH = 7.4), DMEM (pH = 6.0), and DMEM (pH = 6.0, 10 nM GSH) was investigated. RAW 264.7 cells were cultured in a cell culture bottle and exposed to 100 μg mL^{-1}, 200 μL, and no FBS of CTP for 3 h. The cells were placed in fresh DMEM after being well-cleaned with PBS. For the next 4 h, the UV–vis absorbance of the cell supernatant was measured every 30 min. After that, the pH of the DMEM was adjusted to 6.0, and the cell supernatant was collected every 30 min for four tests of UV–vis absorbance. To investigate GSH-triggered drug release, 1 mL of 10 mM GSH solution was added to a cell culture plate. The other experimental steps and detection processes were identical to those described before. For each experiment, 3 mL solution was removed, and 3 mL new DMEM was introduced to maintain the total volume of solution in the culture bottle.

2.13. Penetration and characterization of 3D tumor spheroids

U87 spheroids were formed after 5×10^4 U87-MG cells were seeded on a 96-well spherical microplate for 3 days. 3D tumor spheroids were treated with PBS, CTP, or TMZ (50 μg mL^{-1}), and this mixture was subsequently incubated at 37 °C for 6, 12, 24, 48, and 72 h. The 3D tumor spheroids were washed and mixed with 150 mL of working solution (5 mL Calcein-AM solution (2 mM), 15 mL Hoechst33342 solution (1.5 mM), and 5 mL buffer solution), which was then incubated at 37 °C for 15 min. Finally, fluorescence microscopy was utilized to distinguish living and dead cells (green or blue fluorescence, respectively).

2.14. BBB model establishment and characterization

The BBB model was made of a polycarbonate 12-well transwell membrane with an 8 μm pore size and bEnd.3 cells. The cells were sown at a density of 5×10^4 cells per well and cultivated for three days. An epithelial volt-ohm meter was used to measure the transendothelial electrical resistance of cell monolayers. Only those with values above 200 Ω cm^{-2} were tested. After staining the bEnd.3 cells with DAPI, they were washed in DMEM. The U87-MG cells were cultivated overnight at the bottom of a 12-well plate, with a planting density of 1×10^4 cells/well. In the 3D tumor spheroid group, the U87-MG spheroid was seeded at the bottom of a 12-well plate; the other experimental conditions are all the same. The material was then removed and stained with FITC for 15 min. Then, CTP@RAW (1×10^4 cells/well) in DMEM was injected into the upper chamber and incubated for 12, 24, and 48 h. Finally, a fluorescence microscope was used to examine the distribution of CTP@RAW in the upper chamber and basolateral bottom. In addition, BBB-penetration efficiency was further calculated by fluorescence intensity. Measured the fluorescence intensity of CTP@RAW added into the upper chamber and after 48 h incubation measured the fluorescence intensity of CTP@RAW in the basolateral bottom, then obtained the number of cells crossing the BBB.

2.15. Therapeutic effect investigation of orthotopic glioma

In order to construct the orthotopic glioma model, the nude mice were anesthetized and fixed in the stereoscope frame. In-situ glioma was induced by intraperitoneal injection of U87-MG cells (2×10^5 cells) into the bright lateral striatum. The glioma had grown for a week and was ready for more tests. Tumor-bearing BALB/c mice were randomly assigned to four groups (PBS, free TMZ, CTP, and CTP@RAW). At 7, 10, 13, 16, 19, 22, and 25 days, test groups were intravenously given equal doses of TMZ (5 mg/kg). Throughout the experiment, the weight changes of mice body were monitored, and the fluorescence images were collected at various periods following injection. On the final day of the trial, mice were terminated via cervical dislocation. The heart, lungs, spleen, liver, kidney, and brain were all collected and photographed.

2.16. Semiquantitative and quantitative analysis

Semiquantitative analysis of inflammatory factors (GFAP, Ki67, and Caspase-3) from immunohistochemical staining of tumor-bearing mice was performed using the following calculating process: A fluorescence microscope was used to record luminescence images from immunohistochemical staining. The target areas were selected from luminescence photographs, and the gray values were read using Andor Solis software. The histogram and statistical analysis were drawn using the Origin program and Microsoft Excel.

After centrifugation, the brain tissue supernatant was extracted and homogenized in PBS at a pH of 7.4. The ELISA reagents were then added to the standard sample solutions and incubated for 30 min at 37 °C. Then, either from tissue homogenates or serum, the brain tissue

supernatant was added. The microplate reader was utilized to measure the absorbance at 450 nm. GFAP, TNF-α, and caspase-3 concentrations were ascertained using the pre-established standard curve.

2.17. In vivo safety evaluation

Following therapy, the heart, spleen, liver, kidney, lung, and brain tissues from tumor-bearing mice were collected. They were then promptly preserved in 4 % paraformaldehyde solution for histopathological examination. The tissues were cleaned with PBS. Every sample was divided into 5 μm pieces and embedded in paraffin. The tissue alternations were examined under a microscope after the hematoxylin and eosin (H&E) staining processes were carried out in accordance with the kit's instructions.

2.18. Statistical analysis

The means of each group were reported as the average of three separate experiments plus the standard deviation of the mean, and the statistical significance of any differences between the means was assessed using Student's t-test. At significance levels of $*p < 0.05$, $**p < 0.01$, and $***p < 0.001$, the statistical significance was established.

3. Results and discussion

3.1. Establishment of immune cell targeting-mediated cytomimetic drug delivery system (CTP@RAW)

The CTP nanoparticles were produced using the following approach. CZQDs were first produced using the hydrothermal technique, followed by centrifugal separation. TMZ would be fixed onto the surface of CZQDs by electrostatic contact, while PDA would cling to the surface of CT via dopamine self-polymerization. PDA which wrapped around nanoparticles can prevent TMZ leakage while maintaining the stability of QDs. CZQDs possessed spherical morphology, with diameters of about 7.5 nm and a uniform size distribution, as indicated in the acquired HRTEM image (Fig. 2(a) and (b)). In addition, the CT and CTP sizes were around 8.6 nm and 21 nm, respectively, with a narrow particle size distribution (polydispersity = 0.106 and 0.137) (Fig. 2(b)). The UV–visible spectra and zeta potential might be used to determine if the components were successfully transformed during the functionalization of CZQDs. As illustrated in Fig. 2(c), the UV–vis spectra of TMZ revealed a strong absorption peak at 330 nm, 258 nm, and 212 nm. The UV–vis spectra of CZQDs revealed an acromial absorption peak at 223 nm. The absorption maxima in the UV–vis spectrum of CTP was at 321 nm and 226 nm, while TMZ's absorbance at 258 nm and 212 nm was submerged in the terminal absorption of the CZQDs, confirming the efficacy of TMZ attachment to CZQDs (Fig. 2(c)). The variation of zeta potential on the CZQDs surface also indicated that TMZ and PDA were successfully modified on the CZQDs surface (Fig. S1). CZQDs produce a strong fluorescence emission at 625 nm (Fig. 2(d)). The link between fluorescence intensity and concentration was also investigated. Fig. 2(e) shows a good linear relationship and sensitivity between gray values and CTP concentrations, laying the groundwork for semi-quantitative bioimaging. We immersed the material in PBS, serum and blood with concentrations of 10 % for ten days to determine its stabilities. Finally, we discovered that the fluorescence signal remained constant throughout time, enabling continuous monitoring in a biological environment (Fig. S2). We further tested that CTP particle size remained unchanged in pH 7.4 PBS (Fig. S3). However, the size distribution showed that CTP degraded into 0.7 nm of smaller nanoparticles, and some fragments of polydopamine gathered into large spheres (11 nm and 1300 nm) after incubation with the medium of pH 6.0 (Fig. 2(f)). GSH treatment also led to heavy degrading of CTP, with the diameter changing from 8.6 to 3.1 nm.

The UV–vis spectra of various TMZ dosages were measured and linearly fitted prior to examining the drug loading and release behavior under various settings (Figs. S4 and S5). With an R^2 of 0.9995, the usual working curve was $I = 0.02507\ c_{TMZ} + 0.01123$. It could be found that the drug's loading was pH-dependant, peaking at 54.1 % at pH 8.5, by comparing the loading rates of CZQDs to TMZ (50 μg mL^{-1}) at different pH levels (Fig. S6). The maximum loading rate of CZQDs to TMZ was 46.2 % after 4 h at 50 μg mL^{-1} (pH 8.5), as shown in Fig. S7.

Under various test settings (pH and GSH), the drug release characteristics of CTP were examined. After being loaded into nanoparticles (CTP), only 9.1 % TMZ was dissolved in the pH 7.4 medium after 24 h. When CTP was exposed to a lower pH environment (pH 6.0 and 5.0), the drug release pattern was activated and amplified, resulting in cumulative release percentages of 25.1 % and 35.7 %, respectively (Fig. 2(g)). This phenomenon was caused by the "TMZ-CZQDs" structure's coordination link weakening at lower pH values. This is related to the pH-induced breakdown of the electrostatic attraction between TMZ and CZQDs and the acidic biodegradation of the PDA framework. The tumor cell microenvironment has significantly more GSH than the usual physiological milieu. Enough GSH will cause PDA to break down into monomers, breaking down nanocarriers and drug release. As indicated in Fig. 2(h), with the increasing of GSH concentration, the TMZ release percentage also increased accordingly. According to our research, this process was caused by the breaking of noncovalent hydrophobic connections as well as electrostatic attraction between the aromatic sections of nanocarriers and TMZ. Fig. 2(i) showed the dual-stage responsive TMZ release of CTP performance. The release rate of TMZ from CTP was substantially faster at low pH than at high pH, demonstrating that CTP were pH sensitive. Because an acidic environment surrounds cancer cells, the high drug release in an acidic pH environment promotes cancer cell treatment with CTP, decreasing biotoxicity to normal cells. Moreover, the GSH addition significantly boosted the release rate of TMZ. At pH 5.0, adding 20 μL of 10 mM GSH resulted in a 71.1 % increase in TMZ release compared to without GSH, indicating that CTP is GSH sensitive. When compared to other groups, the rate of drug release from the CTP-affected GSH at pH 6.0 can reach 59.1 %. When pH was 7.4, it reached a drug release rate of 43.2 % with GSH. The above results suggested that because the tumor cell microenvironment is acidic and contains a high amount of GSH, this nanocarrier system was regarded a viable vehicle for drug delivery in cancer therapy.

3.2. Anti-glioma effects of CTP in vitro

Multiple approaches were used to investigate CTP's in vitro anti-glioma efficacy to confirm the improved effects on glioma. As illustrated in Fig. 2(j), Calcein-AM/PI double labeling was used to observe the anti-glioma action in vitro intuitively. After 24 h of incubation with CTP, CT, and TMZ, cells died at varying rates compared to those incubated with blank culture medium (control). We first discovered CTP uptake in U87-MG cells. Fig. S8 shows that the fluorescence signal intensity of the CTP, CT, and CTP groups steadily rose with increasing incubation time. However, no fluorescence signal was found in the TMZ group. After 24 h, free TMZ and CT produced similar numbers of dead cells, which were lower than CTP. CTP produced massive dead cells, displaying the highest cytotoxicity on U87-MG cells. However, CZQDs did not cause cell death, suggesting that the inhibition of cell activity by CTP and CT was due to TMZ release rather than CZQDs toxicity.

Next, an MTT assay was applied to investigate the inhibition effect of CTP on the proliferation of U87-MG cells (Fig. 2(k)). When containing the same dose of TMZ, the inhibitory rate of CTP on the activity of U87-MG cells was similar to that of free TMZ, which indicated that the surface modified PDA of the clinical material CT did not affect the release of TMZ. This further demonstrated that PDA could be decomposed and released TMZ under the condition of low pH and high GSH of tumors. CT also showed similar inhibition rates on U87-MG cells, mainly due to the direct contact of TMZ on the surface of CZQDs. The IC50 was calculated to be 160 μg mL^{-1} of CTP, CT and TMZ, without significant difference.

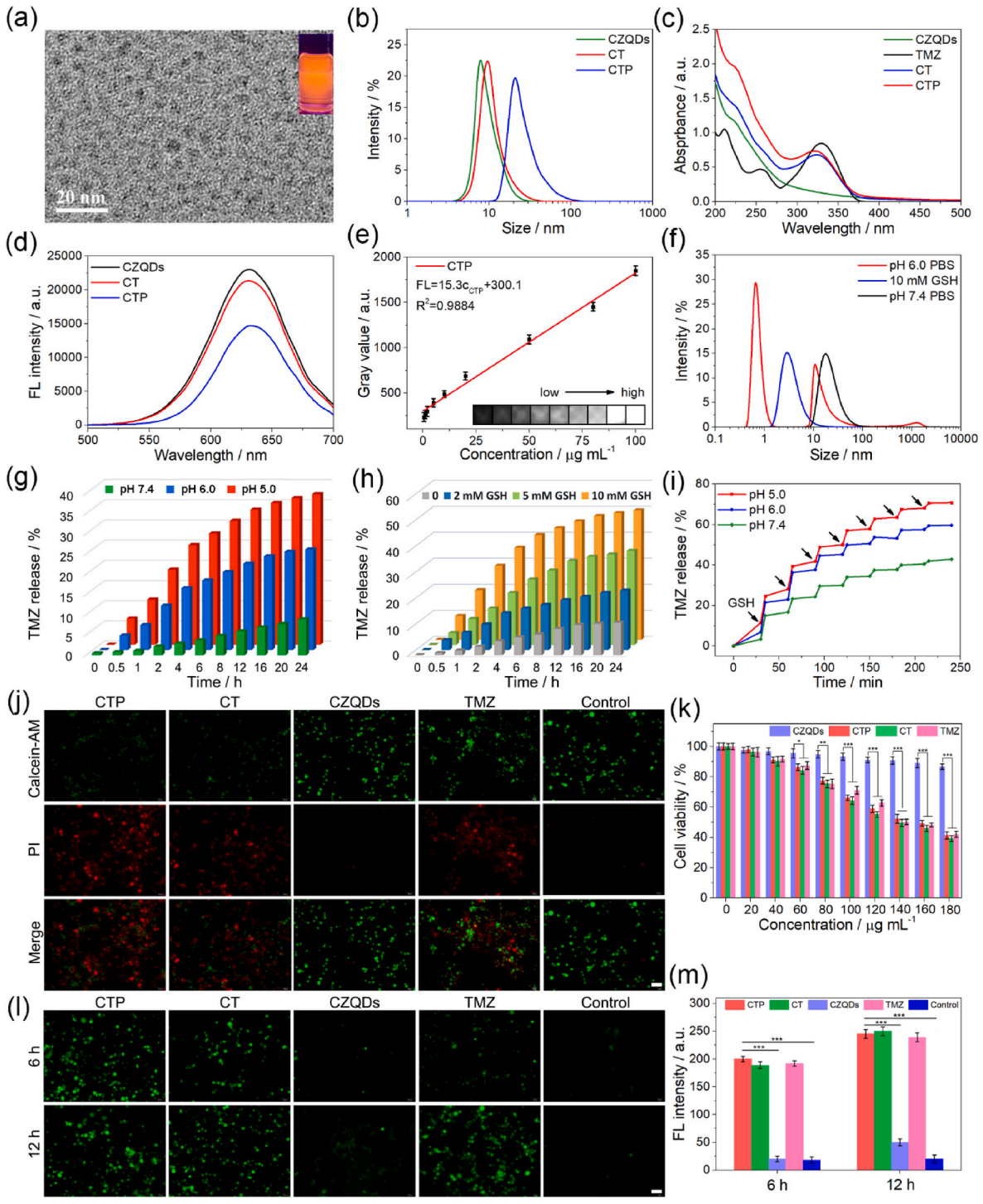

Fig. 2. The characteristics of CTP and validation of its antitumor efficacy in vitro. (a) TEM image of CZQDs. (b) Size distributions of CZQDs, CT and CTP in PB S (pH 7.4) was monitored by dynamic light scattering. (c) UV–vis spectrums of CZQDs, CT and CTP. (d) Fluorescence spectrums of CZQDs, CT and CTP. (e) The average gray values of CTP with different concentrations in each well, insert was the fluorescence imaging. (f) size distribution of CTP response to different pH (6.0, 7.4) and GSH (10 mM), respectively. (g) TMZ release triggered with different acidity PBS (pH 5.0, 6.0 and 7.4). (h) The TMZ release triggered with different GSH concentrations. (i) Dual-staged TMZ release triggered with different acidity and 10 mM GSH. (j) Fluorescence images of Calcein AM (green, live cells, λex = 488 nm) and propidium iodide (red, dead cells, λex = 543 nm) costained U87-MG cells after CTP, CT, CZQDs or TMZ treatments (scale bar: 50 μm). (k) Cell viabilities of U87-MG cells after different nanomaterial treatments. (l) ROS generation in U87-MG cells under various treatments (scale bar: 50 μm). (m) Semi-quantification of ROS generation in U87-MG cells with different treatment group. *p < 0.05, **p < 0.01, ***p < 0.001. (For interpretation of the references to colour in this figure legend, the reader is referred to the Web version of this article.)

However, CZQDs showed good cellular activity, indicating that ZnS and GSH modified on the surface of $CuInS_2$ quantum dots reduced cells toxicity, thereby increasing the material's biocompatibility.

ROS-induced cell death is a common target for tumor therapy. Increased ROS levels cause apoptosis by causing damage to the organelles, membrane structure, and nucleus of the cell. ROS production of CTP, CT, CZQDs, and TMZ after co-incubation with U-87 MG cells was detected by DCFH-DA: the more cells apoptosis, the more ROS produced, and the higher fluorescence intensity. As demonstrated in Fig. 2(l), compared to the control and CZQDs groups, the ROS levels of the CTP, CT, and TMZ groups were significantly higher. They had a time-dependent effect, with the ROS level in the CTP group changing the most. The fluorescence intensity bar graph (Fig. 2(m)) showed that there were significant differences between CTP and CZQDs, $p < 0.001$ and $p < 0.001$, respectively, indicating that CTP had the best therapeutic effect among many materials and excellent potential to treat tumor.

3.3. *In vitro anti-glioma effects towards 3D tumor model*

A 3D tumor model of U87-MG spheroids was applied to simulate the solid tumor microenvironment (Fig. 3(a)). First, U87-MG cells were inoculated into an U-shaped 96-well plate and grew for 3 days to reach

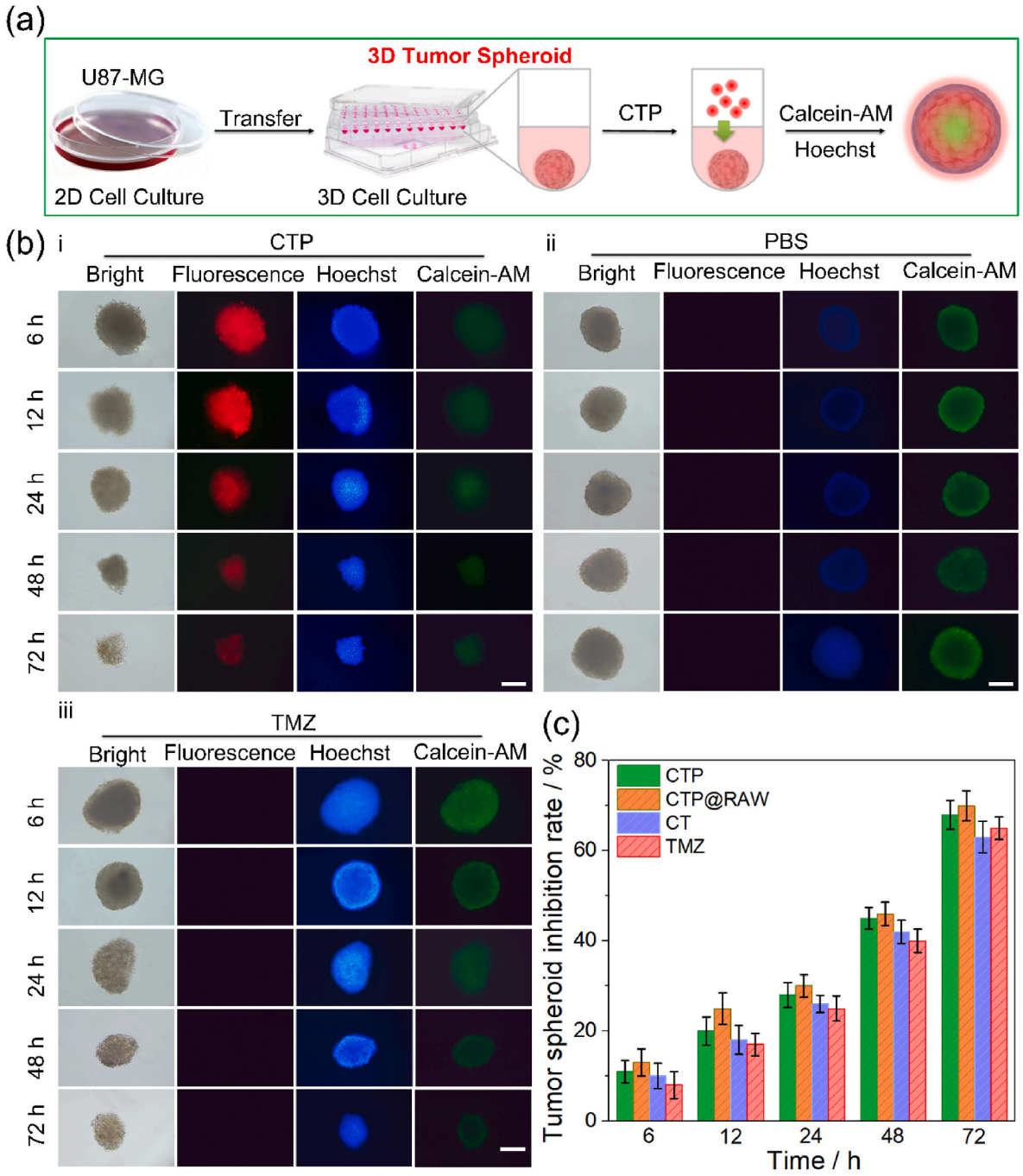

Fig. 3. Anti-glioma effects in vitro towards 3D tumor model. (a) Schematic illustration of therapeutic for 3D U87-MG spheroids. (b) Fluorescence images of Calcein-AM (green) and Hoechst33342 (blue) containing 3D tumor spheroids after CTP, TMZ or PBS treatment (scale bar: 200 μm). (c) 3D tumor spheroids inhibition rate after CTP, CTP@RAW, CT or TMZ treatment of 72 h. (For interpretation of the references to colour in this figure legend, the reader is referred to the Web version of this article.)

the size required for the experiment (about 500 μm in diameter), as shown in Fig. S9. Then, CTP, CTP@RAW, CT or TMZ were added to the experimental group, and PBS was added to the control group. Calcin-AM/Hoechst33342 double staining was used to visually observe the inhibitory effects of CTP, CTP@RAW, CT or TMZ on 3D tumor spheroids. Red fluorescence represented the fluorescence signal of quantum dots presented by CZQDs, green represented living cells, uniformly blue represented normal cells, and bright blue represented apoptotic cells. As shown in Fig. 3(b) and Fig. S10, CT, CTP, CTP@RAW and TMZ induced similar U87-MG cell apoptosis, which appeared in large areas of bright blue compared with the control group. CT and CTP reduced the size of the tumor spheroids to 210 μm and 221 μm, slightly smaller than treated group, due to the enrichment of TMZ by nanoparticles. In CTP@RAW group, the 3D tumor spheroids size riched to 218 μm, Therefore, although CTP was encapsulated in RAW264.7 cells, it did not affect its drug release in the tumor environment, and there was no significant difference. However, the 3D tumor spheroids did not decrease in the control group but slightly increased. In the treatment period, the diameter of U87-MG spheroids was measured, as shown in Fig. S11, consistent with the observed fluorescence imaging. After 72 h of administration, the inhibition rate of 3D tumor spheroids in various groups was measured; CTP, CTP@RAW, CT or TMZ treatment resulted in similar inhibition of glioma, with inhibition rates of 68.5 %, 70.3 %, 63.8 % and 65.1 % (Fig. 3(c)). As a result, the effect of CT, CTP and TMZ on three-dimensional U87-MG spheroids were similar to the results of 2D U87-MG cells, demonstrating that CT and CTP were highly cytotoxic to glioma cells and the tumor spheroids.

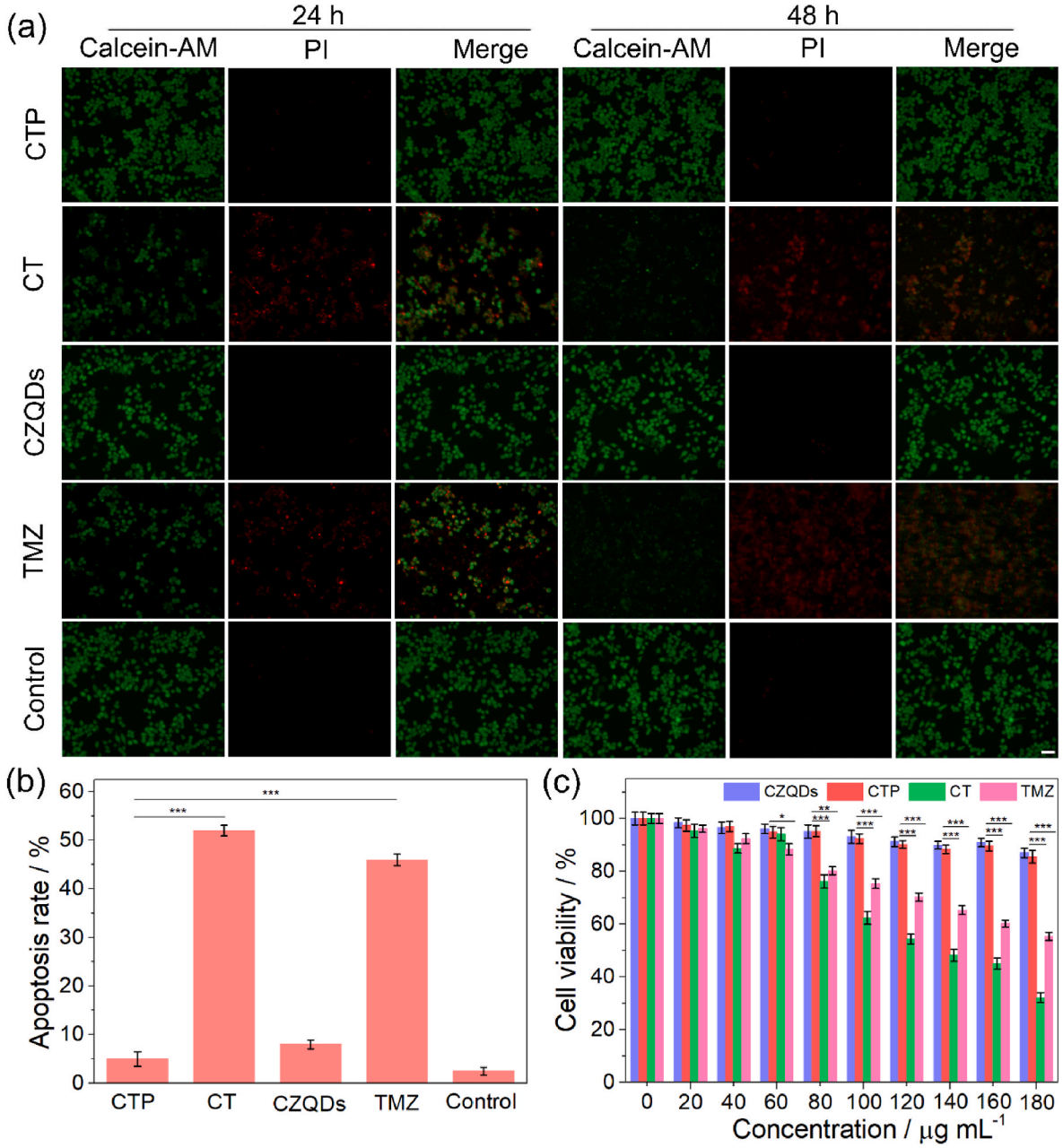

Fig. 4. Toxicity of CTP to RAW264.7 cells. (a) The fluorescence imaging of RAW264.7 cells after co-incubating CZQDs, CT, TMZ or CTP with the Calcein-AM/PI for 24 h and 48 h (scale bar: 50 μm). (b) Statistical apoptosis rate of Calcein-AM/PI staining RAW264.7 cells after exposed to CZQDs, CT, TMZ or CTP for 48 h. (c) Cytotoxicity assessment of CZQDs, CT, TMZ and CTP. *$p < 0.05$, **$p < 0.01$, ***$p < 0.001$.

3.4. RAW264.7 cellular uptake of CTP and its mechanism

One of the critical metrics for assessing the safety of medication nanocarriers is their cytotoxicity. Cells were treated with TMZ, CZQDs, CT, or CTP for 24 and 48 h, after which they were stained with calcein-AM and PI to confirm the biological toxicity of these substances to the cells. Fig. 4(a)'s fluorescence imaging results showed that CZQDs treatment group had no toxicity to RAW264.7 cells, and the results were the same as the control group. Both TMZ and CT treatment groups showed high cytotoxicity, which may be due to the direct contact of TMZ with cells. However, the CTP treatment group showed less cytotoxicity due to the coated PDA on CT, which reduced the chance of direct contact between TMZ and cells and increased biosafety. A high cell survival rate was maintained after 48 h of co-incubation, which showed different cytotoxicity compared with U87-MG (as illustrated in Fig. 4(a)), further indicating that CT modified PDA could only be destroyed by tumor cells to release drugs to damage cells. After incubation for 48 h, the apoptosis rate was statistically measured. As shown in Fig. 4(b), the apoptosis rate of CTP was less than 10 %, while the apoptosis rate of CT and TMZ were 52.03 % and 46.13 %, with a significant difference ($P < 0.001$). In addition, RAW264.7 cells were evaluated for TMZ, CZQDs, CT, and CTP cytotoxicity in vitro by commonly used MTT assay. As shown in Fig. 4 (c), TMZ and CT showed strong cytotoxicity at 80 μg mL^{-1}, while the CTP group showed lower cytotoxicity even when the concentration reached to 180 μg mL^{-1}. The survival rates at high concentration were 85.51 % (CTP), 32.32 % (CT) and 55.26 % (TMZ), respectively, with a significant difference ($P < 0.001$). These results indicate that CT coating modified PDA can enhance the material's biocompatibility and reduce cytotoxicity, providing an excellent cellular carrier for the delivery of therapeutic drugs.

In order to study the uptake behavior of RAW264.7 cells, media containing CZQDs, CT, and CTP were co-cultured with cells, which determined the uptake capacity of RAW264.7 cells to different materials. The fluorescence imaging further visualized the uptake results; fluorescence of the CZQDs was conducted based on their distinguished red light. After incubation of RAW264.7 cells with CZQDs, CT and CTP for 3 h, we observed bright fluorescence in the cytoplasm and the cells' structure were intact, indicating that CZQDs, CT and CTP could be taken up by RAW264.7 cells, further demonstrating the success of our synthesized drug delivery system (Fig. S12). RAW264.7 is a type of innate immune cell and phagocyte, which can effectively uptake nanoparticles through phagocytosis. This phagocytosis depends on the binding of membrane surface receptors (such as scavenger receptors, toll-like receptors, and complement receptors) to nanoparticles [59–61]. As shown in Fig. 5(a) that the fluorescence intensity increased with the increase of incubation time, and the fluorescence reached its strongest after 3 h of coincubation. The fluorescence study showed that cells absorbed CTP in a temporal gradient, reaching equilibrium (48.4 %) at 3 h, showing time dependence. This allowed researchers to examine the absorption differences between CT and CTP by RAW264.7 cells (Fig. 5(b)).

The camouflaged nano-complex CTP@RAW was obtained through in vitro co-incubation. As shown in Fig. 5(c), the intracellular loading dynamics were examined over an extended period at various CTP doses. The loading ratio analysis demonstrated that the absorption of CTP by cells happened in a time-dependent way, with the highest percentage of cells (51.7 %) absorbing the substance at 3 h when the concentration of CTP was 100 μg mL^{-1}. The uptake rate stayed saturated after that. The loading ratio dropped to 20.3 % at 50 μg mL^{-1} of CTP, demonstrating concentration dependence. Furthermore, the retention ratio of CTP in RAW cells remained high (82.9 %) at 48 h in DMEM, as shown in Fig. 5 (d). Thus, the above demonstrated that CTP@RAW was assembled successfully and provided an excellent potential for long-term monitoring.

The effective release of medications is an essential aspect of illness treatment. TMZ has been shown to be released from CTP in the presence of low pH or high GSH concentration, and we then further investigated the drug release of CTP@RAW as follows. Fig. S13 showed different TMZ release ratios of CTP@RAW in DMEM with different pH, up to 36.4 % at the pH of 5.0. A high concentration of GSH could also increase the ratio of CTP@RAW releasing TMZ. In the medium containing 10 mM GSH, the TMZ release rate was as high as 49.5 % (Fig. S14). To demonstrate that our designed CTP@RAW can release TMZ within the tumor, we adopted pH 6.0 DMEM and 10 mM GSH to simulate the tumor microenvironment. According to the dual-stage responsive TMZ release performance results, the passive TMZ release nearly reached a plateau in 4 h. However, when the DMEM with pH of 6.0 was changed, the TMZ release significantly accelerated. After adding GSH, a further expedition of TMZ release was noticed 3 h after addition (Fig. 5(e)). Finally, to demonstrate that CTP@RAW could release TMZ in a tumor environment, as shown in Fig. 5(f). We incubated CTP@RAW with RAW264.7 cells or U87-MG cells, and it was observed that more TMZ was released in U87-MG cells (52.2 %) than in RAW264.7 cells (10.3 %). These findings supported the prepared CTP@RAW's ability to react to the tumor environment and initiate appropriate on-demand drug release.

3.5. BBB crossing ability of CTP@RAW in vitro

For brain tumors to be effective, CTP@RAW must have a robust BBB-crossing ability, which is typically confirmed by a transwell penetration assay. A polycarbonate 12-well transwell membrane with 8 μm pore size was used to build the BBB model and bEnd.3 cells were planted on it. U87-MG cells were then seeded into the basolateral bottom of the transwell plate. The upper chamber then received CTP@RAW. Lastly, a fluorescent microscope was used to assess CTP@RAW's BBB crossing capabilities in vitro (Fig. 5(g) i). As anticipated, U87-MG cells labeled with FITC were located near the basolateral bottom of the transwell plate (Fig. S15). More significantly, red fluorescence of CTP@RAW with intact morphology was also detected from the additional CTP@RAW in the upper chamber of the transwell (Fig. 5(h) i). Then the BBB-penetration efficiency was obtained (38.8 %) by fluorescence intensity measuer. There was no red fluorescence in the transwell plate of the control group, where RAW cells were seeded and labeled with FITC (Fig. S16). In the control groups, which could be observed that U87-MG is stained with green fluorescence in the basolateral bottom of the transwell plate, but almost no red fluorescence appeared (Fig. S17). Using tumor cytokines as chemotaxis, CTP@RAW was able to pass through bEnd.3 cell monolayers, according to the data. At 48 h, it was challenging to observe the complete morphology of U87-MG cells, indicating that the dropped CTP@RAW could kill U87-MG cells and exert anti-tumor properties.

3D tumor spheroids can be better used to simulate tumor characteristics, so we used 3D tumor spheroids to demonstrate further the ability of CTP@RAW to cross BBB. First, 3D tumor spheroids stained with FITC were placed on the bottom of the transwell plate, and CTP@RAW was added to the upper chamber; CTP@RAW was observed in the lower chamber, as shown in Fig. 5(g) ii. In Fig. 5(h) ii, it could be observed that CTP@RAW emitting red fluorescence also appeared in the lower chamber, the same as the above experimental results. At 24 h, it was found that CTP@RAW was more than that at 12 h, and CTP@RAW mostly surrounded the tumor spheroid, as shown in Fig. S18. At 48 h, CTP@RAW increased further, the invasion of CTP@RAW loosened the tumor ball, and many fragments were dropped. While, it could not be observed that CZQDs, CT, or CTP emitting red fluorescence also appeared in the lower chamber (Fig. S19), the same as the above 2D cell experimental results. According to the above experimental results, it could be concluded that CTP@RAW had a unique ability in penetrating the BBB. In addition, TNF-α was detected in the lower chamber supernatant after CTP@RAW was added for 12, 24, and 48 h. As shown in Fig. 5(i), with more and more CTP@RAW crossing into the bottom of the transwell plate, the content of TNF-α is decreasing, indicating that CTP@RAW could release TMZ and play a therapeutic role. These results demonstrated that CTP@RAW could penetrate the bEnd.3 cell

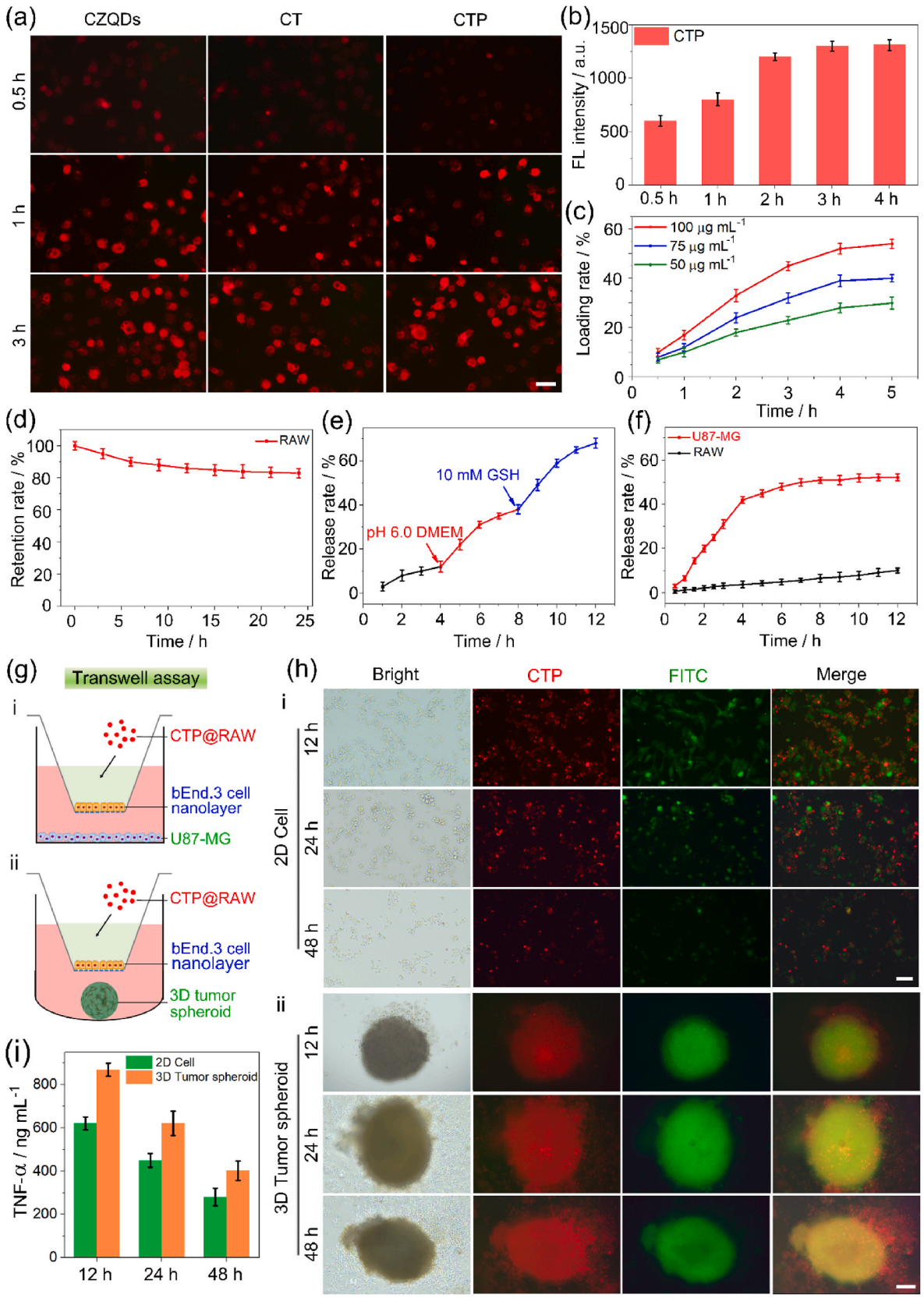

Fig. 5. The CTP loading by RAW264.7 cells and the BBB-crossing ability of CTP@RAW. (a) Fluorescence imaging of RAW264.7 cells with the treatment of CZQDs, CT and CTP after 0.5 h, 1 h and 3 h. Scale bar: 20 μm. (b) Semi-quantification of fluorescence intensity in RAW264.7 cells in different treatment group. (c) The loading efficiency of CTP with different concentrations in RAW264.7 cells. (d) The retention rate of CTP in RAW cells. (e) Tual-staged TMZ release triggered with pH 6.0 DMEM and 10 mM GSH. (f) TMZ release rate of CTP@RAW in the medium contain RAW264.7 cells or U87-MG cells. (g) Schematic depiction of BBB model formation in vitro and CTP@RAW transit through the BBB. (h) Fluorescence imaging on the basolateral bottom of the transwell plate after various treatments (scale bar = 100 μm). (i) Detection of TNF-α in U87-MG cells and 3D tumor spheroids in transwell plate.

monolayer, increasing the effectiveness of CTP in crossing the BBB and being essential for managing orthotopic glioma.

3.6. In vivo anti-glioma effects towards orthotopic glioma xenograft model

Inspired by CTP@RAW's exceptional performance, orthotopic BALB/c nude mice models with U87-MG xenograft tumors were created in order to investigate CTP@RAW's anti-glioma therapeutic efficacy. Every three days, intravenous administration of CTP@RAW, Free TMZ, Free CPT, and PBS was carried out via tail vein and imaging. Seven dosages in total were administered (Fig. 6(a)). After I.V. injection, the in vivo fluorescence imaging was determined every 3 h, which showed the highest fluorescence intensity at the point of post-injection of 9 h, and the brain signals could be traced for up to 48 h (Fig. S20). During the subsequent treatment period, we selected 9 h after I.V. injection CTP@RAW or CTP as the time point for brain signal acquisition. Fig. 6 (b) displays representative brain fluorescence pictures of orthotopic U87-MG xenograft nude mice, illustrating the targeted administration of the encapsulated medicines. Mice were sacrificed 48 h after injection, and the brain and primary organs were separated for ex vivo fluorescence imaging and quantitative biodistribution analysis. Compared with the free CPT group, the brain in CTP@RAW groups showed significantly higher fluorescence signals, although some level of fluorescence signals was observed in the liver because of uptaken of CTP@RAW by reticuloendothelial systems (Fig. 6(c)). Mice were slaughtered 48 h after injection, and the brain and primary organs were isolated for ex vivo fluorescence imaging and quantitative biodistribution analysis. Though fluorescence signals were also found in the liver due to CTP@RAW uptake via reticuloendothelial systems, CTP@RAW groups had significantly larger fluorescence signals in the brain than the free CPT group (Fig. 6(c)). Then the brain's average fluorescence intensity of each group was semi-quantified (Fig. 6(d)), which showed that CTP@RAW could target tumor sites and display bright fluorescence even though the tumors were located deep in the brain covered by the skull. The fact that there was no discernible difference in the mice's weight between the CTP@RAW, CTP, and PBS treatment groups for the course of the treatment indicates that the experimental treatments were well tolerated at the test dose (Fig. 6(e)). Mice survival was tracked and documented. After receiving CTP@RAW therapy, the mice had the best survival rate (Fig. 6(f)). The PBS group had a median survival time of 40 days; whereas, the CTP@RAW group had a considerably longer median survival time of 80 days (***$p < 0.001$, tested by Log-rank analysis). Compared with the free TMZ group, the median survival time was 60 days, but the mice's body weight significantly decreased due to the toxicity of TMZ (Fig. 6(e)). These results demonstrated that CTP@RAW had the opportunity to target and deliver TMZ to glioma and had long-term time visualization for glioma.

Brain tissue was extracted for immunohistochemistry and H&E staining to elucidate the contribution of CTP@RAW to orthotopic glioma. Brains were removed on Day 28 and paraffin slices were prepared for H&E staining. Tumor cells were denser and darker than normal cells, according to an H&E staining examination (Fig. 7(a)). The CTP@RAW group's glioma area was less than the other groups (Fig. S21). The H&E stained area on Day 28 was used to calculate the glioma inhibition rate in each group following the delivery of seven doses. Glioma was most

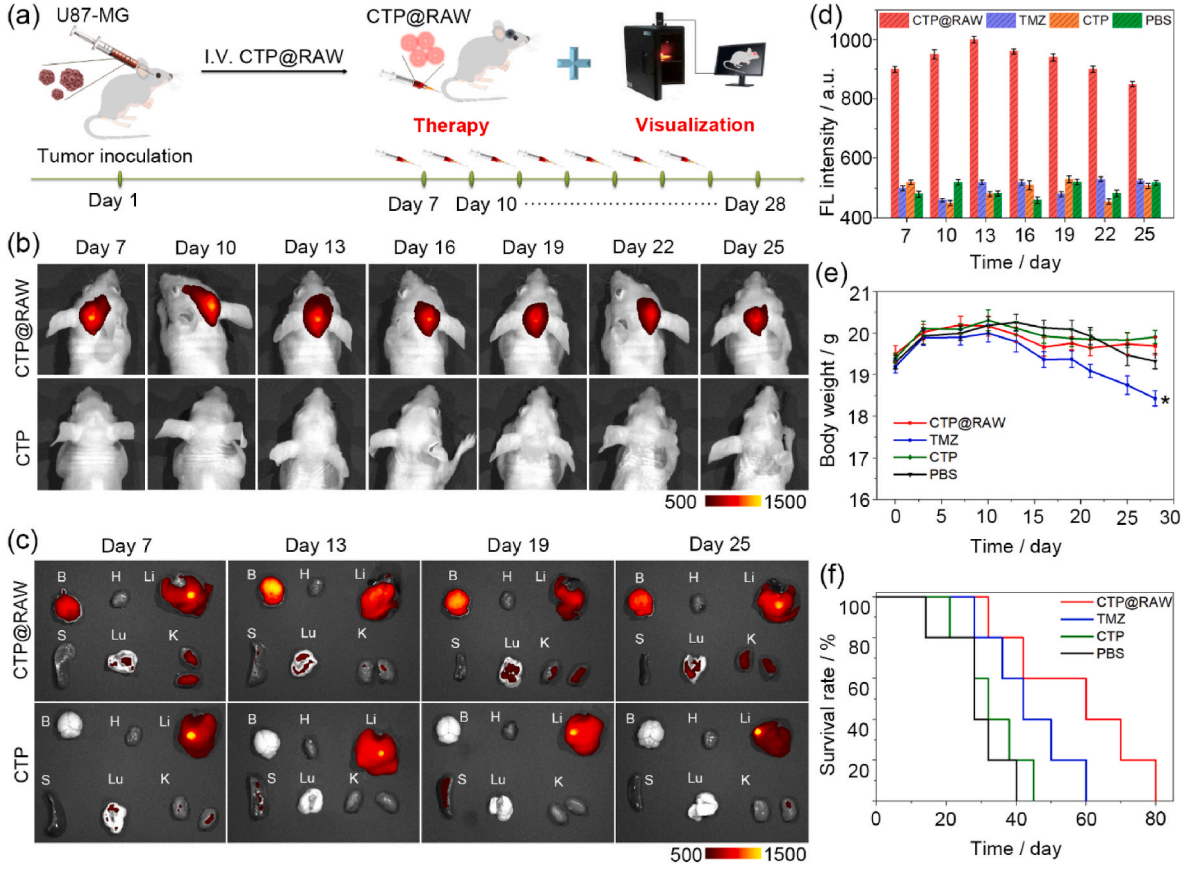

Fig. 6. Visualization and therapy effect of orthotopic glioma. (a) Schematic illustration of therapeutic schedule for orthotopic BALB/c nude mice bearing U87-MG xenograft tumors. (b) In vivo brain fluorescence imaging of orthotopic U87-MG xenograft nude mice in CTP@RAW and CTP groups. (c) Ex vivo vital organs (brain, heart, liver, spleen, lung and kidneys) of orthotopic U87-MG xenograft nude mice in CTP@RAW and CTP groups. (d) Semi-quantification of fluorescence intensity in brain of orthotopic U87-Luc xenograft nude mice with the treatment of PBS, TMZ, CTP@RAW and CTP. (e) Body weights of orthotopic U87-MG xenograft nude mice over time. (f) Survival curves and median survival time of different groups. Data are presented as mean ± SD (n = 5). *$p < 0.05$.

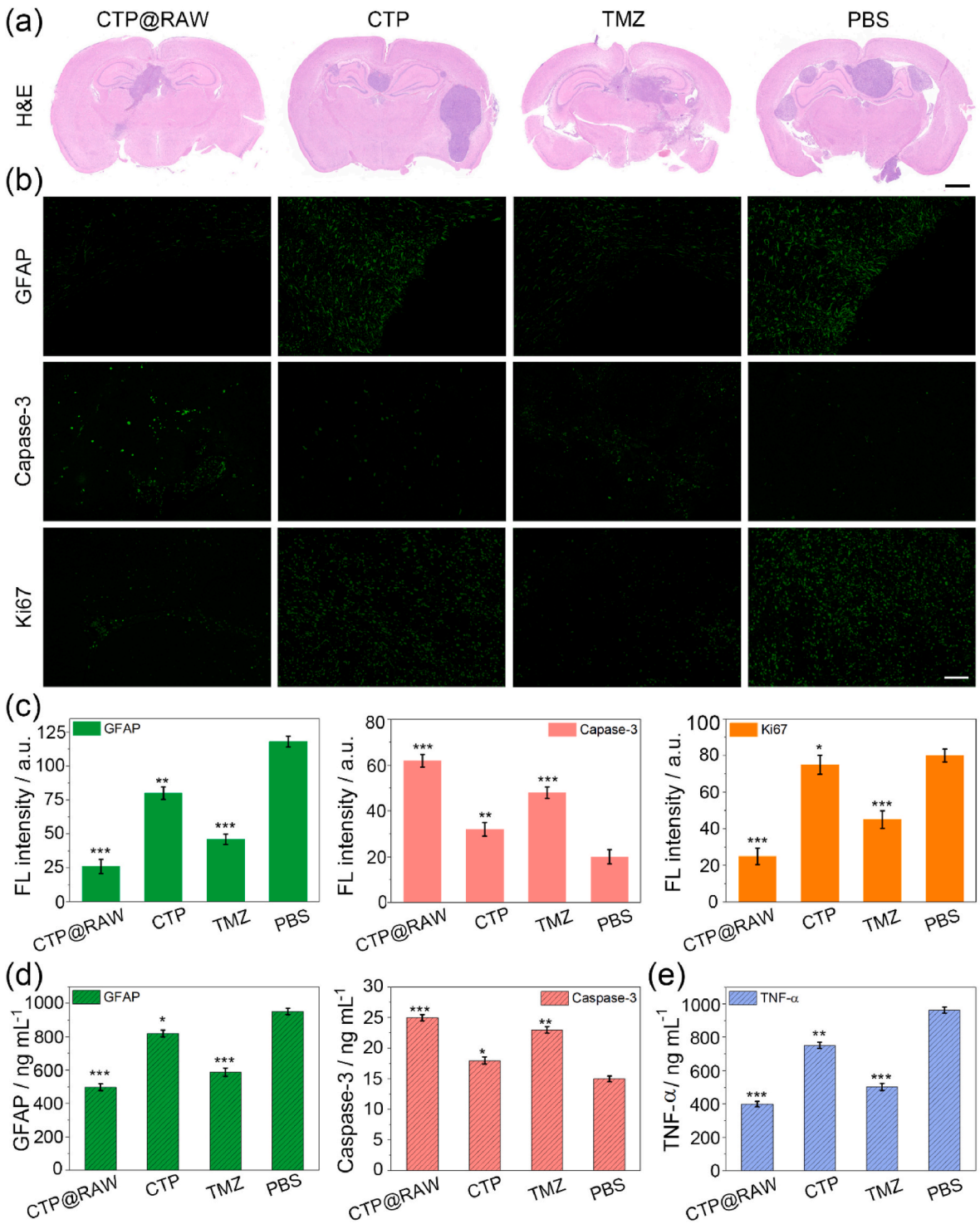

Fig. 7. Mechanisms of therapeutic efficacy towards glioma in vivo. (a) H&E staining of brain tissues in different groups. Scale bar: 1000 μm. (b) The immunofluorescent staining images of GFAP, Capase-3 and Ki67 in glioma regions. Scale bar: 200 μm. (c) Immunohistochemical semi-quantitative examination of GFAP, Capase-3 and Ki67 levels in brain tissue after treatment. (d) Quantitative analysis of GFAP and Capase-3 in brain tissue homogenate supernatant. (e) Quantitative analysis of TNF-α in brain tissue homogenate supernatant. Three measurements were averaged. *p < 0.05, **p < 0.01. ***p < 0.001.

inhibited by CTP@RAW treatment, with an inhibition rate of 86.3 % (Fig. S22). The reasion was that the cellular bionic drug delivery system we constructed was to wrap TMZ in RAW cells, utilizing the specific immune homing effect of RAW264.7 cells on tumors to achieve efficient targeting and enrichment of drugs, which realized the high BBB penetration ability of CTP@RAW. The small amount of free TMZ that crossed the blood-brain barrier may be why free TMZ had modest anti-glioma effects in vivo, due to TMZ was a liposoluble molecule small molecule compound with a BBB penetration efficiency of 10 %–20 % [62]. The fact that CTP did not increase the rate of tumor growth inhibition when compared to free TMZ may have been due to the nanoparticles' inability to traverse the blood-brain barrier. After that, brain sections were immunofluorescently stained with DAPI and many antibodies, including GFAP, Caspase-3, and Ki67. Compared to the PBS group, Ki67

expression in tumor regions of the mice treated with CTP@RAW was decreased with the lowest fluorescence intensity, indicating that CTP@RAW treatment significantly prevented glioma cell proliferation. GFAP, a marker of astrocyte activation located at the glioma-normal cell border [63], reduced the greatest in the CTP@RAW group and exhibited the lowest fluorescence intensity, indicating glioma remission. H&E staining intuitively demonstrated CTP@RAW's good inhibitory activity to glioma growth. The improved therapeutic efficacy of CTP@RAW in vivo was further confirmed by immunofluorescent staining of GFAP and Ki67, which was consistent with previous studies. Activation of Caspase-3 causes specific morphological and biochemical changes in apoptotic cells, which is considered a sign of apoptosis and plays an irreplaceable role in apoptosis [64]. As shown in Fig. 7(b), Caspase-3 showed the highest fluorescence intensity in CTP@RAW-treated tumors. Furthermore, semi-quantitative statistics of the mean fluorescence intensity of Ki67, GFAP, and Caspase-3 revealed significant differences between the CTP@RAW group and the other control group, showing that CTP@RAW had a strong therapeutic effect on glioma (Fig. 7(c)).

Quantification of different cytokines (GFAP, Caspase-3 and TNF-α) was investigated by ELISA. Following centrifugation, the blood and brain tissue supernatant were extracted and homogenized in 1 mL of PBS (pH = 7.4). The standard sample solutions were mixed with the ELISA reagents, and the mixture was then incubated for 30 min at 37 °C. The serum or brain tissue supernatant was then added. Using a microplate reader, the absorbance at 450 nm was quantified. The developed standard curve was used to calculate the concentrations of various cytokines. The activity of GFAP and Caspase-3 in all groups was decreased to varying degrees compared to the PBS group. The level of GFAP and Caspase-3 post-administration of CTP@RAW was sharply decreased in brain tissue supernatant (Fig. 7(d)) and serum (Figs. S23 and S24). The downregulation of GFAP and Caspase-3 in tumor tissues was found to be associated with the higher therapeutic efficacy of CTP@RAW against glioma, as evidenced by the expression of these two proteins in tumor tissues being in step with trends of anti-glioma effects in vivo. Macrophages and monocytes mainly produce pro-inflammatory cytokine TNF-α and play a role in tumor alterations and inflammatory responses [65]. The upregulation of TNF-α in brain tissue homogenate supernatant (Fig. S25) and serum (Fig. 7(e)) caused by inflammation was successfully suppressed by CTP@RAW, indicating that CTP@RAW was more effective than TMZ and CTP in reducing the number of inflammatory cytokines secreted.

The ELISA results led us to the following conclusions: APD@RAW could be recruited to cross the BBB and accumulate in the tumor site due to the homing effect of RAW, and the released TMZ exerts a therapeutic effect on glioma under the around condition with low pH level and high GSH concentration. All of these have also shown that this drug delivery system dramatically improves the delivery efficiency and ultimate therapeutic effect of TMZ drugs.

3.7. *In vivo toxicity evaluation*

Future applications of cellular drug delivery technology may be influenced by its in vivo safety performance. Following seven dosages, we investigated H&E-stained liver, kidney, lung, and heart sections in mice to see if CTP@RAW was detrimental to the significant organs during in vivo body metabolism. Every organ in the CTP@RAW group and the PBS group, as seen in Fig. 8, had a distinct texture and lacked any overt pathological indicators, such as necrosis, edema, or inflammation. This was a positive indication that the drug-loaded intelligent system had no detrimental effects on the organism's metabolism. TMZ can induce severe damage to the kidney and liver tissue, which could cause renal tubules to be injured and hepatocyte aggregation. However, in the CTP group, we could not find the abnormal cells in kidney and liver tissue, indicating that CTP could effectively encapsulate TMZ to prevent drug leakage and avoid direct contact between TMZ and tissues. The medication put on CTP@RAW was nearly entirely released into the brain as a result of the constant, sporadic near-infrared light radiation, and reduce physical toxicity by reducing the concentration of TMZ in the blood. Long-term brain retention of CTP@RAW resulted in extended drug action duration, increased medication efficacy, avoided the onset of dangerous side effects in metabolism, and kept the drug's concentration within a safe range during the metabolism.

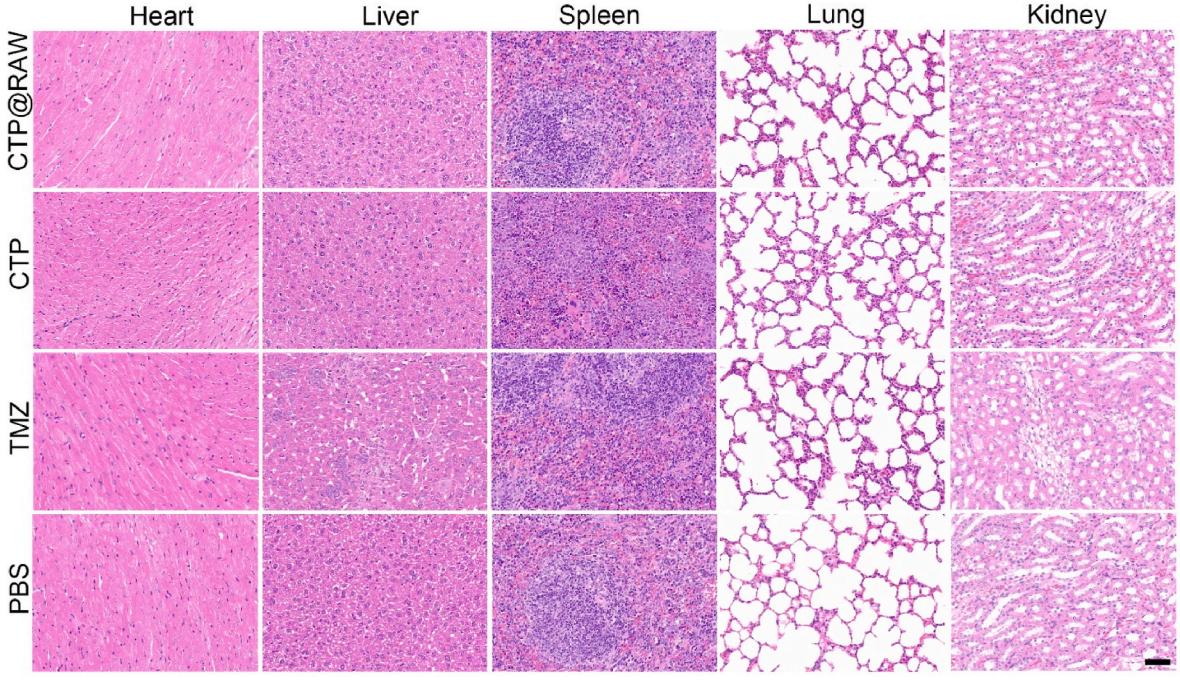

Fig. 8. The toxicity evaluation of the drug delivery system to mice. H&E staining of the heart, liver, spleen, lung and kidney tissues from all the groups after treatment. Scale bar: 100 μm.

4. Conclusions

In summary, we de developed a novel cellular biomimetic drug delivery system (CTP@RAW) with macrophage camouflaged diagnostic and therapeutic nanoparticles as a strategy. This system can penetrate the BBB and target-enriched at the glioma site for controlled drug release, precision therapy, and visualization. Our synthesized drug delivery system can simultaneously target visualization probes and therapeutic drugs to the tumor site by exploiting the specific immune homing ability of RAW264.7 cells. CZQDs core enables precise localization and real-time visualization of brain parenchymal tumors under the skull overlay, and PDA-modified CT diagnostic nanoparticles reduce the risk of damage to the carrier. CTP could be disassembled to release the therapeutic drug TMZ in an in situ glioma model under the tumor microenvironment with low pH and high glutathione concentration. Thus, CTP@RAW demonstrated a superior ability to cross the blood-brain barrier and illuminate even the subcranial tumor region. The released TMZ from them inhibited tumor growth in vivo and modulated the expression levels of GFAP, Ki67, Caspase-3, and TNF-α, suggesting that it is an effective drug delivery for the systemic diagnosis and treatment of gliomas. Overall, this work provides an advanced, intelligent, immune cell-camouflaged diagnostic and therapeutic drug delivery system, CTP@RAW, which shows promising applications in BBB penetration, real-time visualization, and precision therapy.

CRediT authorship contribution statement

Xiu Wang: Writing – original draft, Methodology, Funding acquisition, Formal analysis, Data curation. **Baoqin Song:** Investigation, Data curation. **Mengru Wu:** Data curation. **Lijing Qin:** Visualization. **Wanjun Liang:** Writing – review & editing, Supervision, Project administration, Funding acquisition, Conceptualization.

Ethics approval and informed consent

The animal procedures were performed in compliance with the recommendations of the Institutional Animal Care and Use Committee at the School of Pharmacy and Pharmaceutical Sciences and Institute of Materia Medica at Shandong First Medical University.

Declaration of competing interest

The authors declare the following financial interests/personal relationships which may be considered as potential competing interests: Wanjun Liang reports financial support was provided by Natural Science Foundation of Shandong. Wanjun Liang reports financial support was provided by Taishan Scholars Program. Wanjun Liang reports financial support was provided by Joint Innovation Team for Clinical & Basic Research. If there are other authors, they declare that they have no known competing financial interests or personal relationships that could have appeared to influence the work reported in this paper.

Acknowledgments

We gratefully acknowledge financial support from the Natural Science Foundation (ZR2022QB232, ZR2023MC050), the Academic promotion program of Shandong First Medical University (No. 2019LJ003), the Taishan Scholars Program (tsqnz20231237), and Joint Innovation Team for Clinical & Basic Research (202401).

Appendix A. Supplementary data

Supplementary data to this article can be found online at https://doi.org/10.1016/j.mtbio.2025.101694.

Data availability

Data will be made available on request.

References

[1] M. Weller, P.Y. Wen, S.M. Chang, L. Dirven, M. Lim, M. Monje, G. Reifenberger, Glioma, Nat. Rev. Dis. Primers 10 (2024) 33.
[2] C. Horbinski, T. Berger, R.J. Packer, P.Y. Wen, Clinical implications of the 2021 edition of the WHO classification of central nervous system tumours, Nat. Rev. Neurol. 18 (2022) 515–529.
[3] J.P. Redlich, F. Feuerhake, J. Weis, N.S. Schaadt, S. Teuber-Hanselmann, C. Buck, S. Luttmann, A. Eberle, S. Nikolin, A. Appenzeller, A. Portmann, A. Homeyer, Applications of artificial intelligence in the analysis of histopathology images of gliomas: a review, Imaging 2 (2024) 16.
[4] L.C.S. Erthal, O.L. Gobbo, E.R. Hernandez, Biocompatible copolymer formulations to treat glioblastoma multiforme, Acta Biomater. 121 (2021) 89–102.
[5] M.G. Yonk, M.A. Lim, C.M. Thompson, M.S. Tora, Y. Lakhina, Y. Du, K.B. Hoang, A. M. Molinaro, N.M. Boulis, W. Hassaneen, K. Lei, Improving glioma drug delivery: a multifaceted approach for glioma drug development, Pharmacol. Res. 208 (2024) 107390.
[6] T.J. DePalma, C.L. Hisey, K. Hughes, D. Fraas, M. Tawfik, J. Scharenberg, S. Wiggins, K.T. Nguyen, D.J. Hansford, E. Reátegui, A. Skardal, Tuning a bioengineered hydrogel for studying astrocyte reactivity in glioblastoma, Acta Biomater. 189 (2024) 155–167.
[7] D. Wu, Q. Chen, X. Chen, F. Han, Z. Chen, Y. Wang, The blood-brain barrier: structure, regulation, and drug delivery, Signal Transduct. Targeted Ther. 8 (2023) 217.
[8] B. Song, X. Wang, L. Qin, S. Hussain, W. Liang, Brain gliomas: diagnostic and therapeutic issues and the prospects of drug-targeted nano-delivery technology, Pharmacol. Res. 206 (2024) 107308.
[9] H.Y. Zhang, Y.J. Li, J.Y. Huang, L.M. Shen, Y. Xiong, Precise targeting of lipid metabolism in the era of immuno-oncology and the latest advances in nano-based drug delivery systems for cancer therapy, Acta Pharm. Sin. B (2024), https://doi.org/10.1016/j.apsb.2024.07.021.
[10] J. Xie, Z. Shen, Y. Anraku, K. Kataoka, X. Chen, Nanomaterial-based blood-brain-barrier (BBB) crossing strategies, Biomaterials 224 (2019) 119491.
[11] C. Bérard, C. Truillet, B. Larrat, F. Dhermain, M.A. Estève, F. Correard, A. Novell, Anticancer drug delivery by focused ultrasound-mediated blood-brain/tumor barrier disruption for glioma therapy: from benchside to bedside, Pharmacol. Ther. 250 (2023) 108518.
[12] B. Wang, S. Hu, Y. Teng, J. Chen, H. Wang, Y. Xu, K. Wang, J. Xu, Y. Cheng, X. Gao, Current advance of nanotechnology in diagnosis and treatment for malignant tumors, Signal Transduct. Targeted Ther. 9 (2024) 200.
[13] Y. Zhao, J. Qin, D. Yu, Y. Liu, D. Song, K. Tian, H. Chen, Q. Ye, X. Wang, T. Xu, H. Xuan, N. Sun, W. Ma, J. Zhong, P. Sun, Y. Song, J. Hu, Y. Zhao, X. Hou, X. Meng, C. Jiang, J. Cai, Polymer-locking fusogenic liposomes for glioblastoma-targeted siRNA delivery and CRISPR-Cas gene editing, Nat. Nanotechnol. (2024), https://doi.org/10.1038/s41565-024-01769-0.
[14] S. Zha, H. Liu, H. Li, H. Li, K.L. Wong, A.H. All, Functionalized nanomaterials capable of crossing the blood-brain barrier, ACS Nano 18 (2024) 1820–1845.
[15] G.C. Terstappen, A.H. Meyer, R.D. Bell, W. Zhang, Strategies for delivering therapeutics across the blood-brain barrier, Nat. Rev. Drug Discov. 20 (2021) 362.
[16] X. Wang, X. Hao, Y. Zhang, Q. Wu, J. Zhou, Z. Cheng, J. Chen, S. Liu, J. Pan, Y. Wang, J.B. Fan, Bioinspired adaptive microdrugs enhance the chemotherapy of malignant glioma: beyond their nanodrugs, Adv. Mater. 36 (2024) 2405165.
[17] J. Chen, J. Pan, S. Liu, Y. Zhang, S. Sha, H. Guo, X. Wang, X. Hao, H. Zhou, S. Tao, Y. Wang, J.B. Fan, Fruit-derived extracellular-vesicle-engineered structural droplet drugs for enhanced glioblastoma chemotherapy, Adv. Mater. 35 (2023) 2304187.
[18] J. Li, X. Wang, H. Guo, H. Zhou, S. Sha, Y. Yang, J. Chen, X. Hao, J. Pan, Y. Wang, J.B. Fan, Immunostimulant citrus fruit-derived extracellular vesicle nanodrugs for malignant glioma immunochemotherapy, Chem. Eng. J. 484 (2024) 149463.
[19] W. Niu, Q. Xiao, X. Wang, J. Zhu, J. Li, X. Liang, Y. Peng, C. Wu, R. Lu, Y. Pan, J. Luo, X. Zhong, H. He, Z. Rong, J.B. Fan, Y. Wang, A biomimetic drug delivery system by integrating grapefruit extracellular vesicles and doxorubicin-loaded heparin-based nanoparticles for glioma therapy, Nano Lett. 21 (2021) 1484–1492.
[20] N. Jain, S. Shahrukh, P. Famta, S. Shah, G. Vambhurkar, D.K. Khatri, S.B. Singh, S. Srivastava, Immune cell–camouflaged surface-engineered nanotherapeutics for cancer management, Acta Biomater. 155 (2023) 57–79.
[21] H. Wang, X. Wang, X. Zhang, W. Xu, The promising role of tumor-associated macrophages in the treatment of cancer, Drug Resist. Updates 73 (2024) 101041.
[22] S. Li, X. Meng, B. Peng, J. Huang, J. Liu, H. Xiao, L. Ma, Y. Liu, J. Tang, Cell membrane-based biomimetic technology for cancer phototherapy: mechanisms, recent advances and perspectives, Acta Biomater. 174 (2024) 26–48.
[23] X. Li, X. Geng, Z. Chen, Z. Yuan, Recent advances in glioma microenvironment-response nanoplatforms for phototherapy and sonotherapy, Pharmacol. Res. 179 (2022) 106218.
[24] B. Sethi, V. Kumar, K. Mahato, D.W. Coulter, R.I. Mahato, Recent advances in drug delivery and targeting to the brain, J. Contr. Release 350 (2022) 668–687.
[25] H. Wu, T. Zhang, N. Li, J. Gao, Cell membrane-based biomimetic vehicles for effective central nervous system target delivery: insights and challenges, J. Contr. Release 360 (2023) 169–184.

[26] S.S. Zhang, R.Q. Li, Z. Chen, X.Y. Wang, A.S. Dumont, X. Fan, Immune cells: potential carriers or agents for drug delivery to the central nervous system, Mil. Med. Res. 11 (2024) 19.
[27] X. Wang, B. Song, Z. Wang, L. Qin, W. Liang, The innovative design of a delivery and real-time tracer system for anti-encephalitis drugs that can penetrate the blood-brain barrier, J. Contr. Release 363 (2023) 136–148.
[28] Y. Zhao, J. Chen, M. Andreatta, B. Feng, Y.Q. Xie, M. Wenes, Y. Wang, M. Gao, X. Hu, P. Romero, S. Carmona, J. Sun, Y. Guo, L. Tang, IL-10-expressing CAR T cells resist dysfunction and mediate durable clearance of solid tumors and metastases, Nat. Biotechnol. (2024), https://doi.org/10.1038/s41587-023-02060-8.
[29] H. Liu, H. Lv, X. Duan, Y. Du, Y. Tang, W. Xu, Advancements in macrophage-targeted drug delivery for effective disease management, Int. J. Nanomed. 18 (2023) 6915–6940.
[30] T. Liang, R. Zhang, X. Liu, Q. Ding, S. Wu, C. Li, Y. Lin, Y. Ye, Z. Zhong, M. Zhou, Recent advances in macrophage-mediated drug delivery systems, Int. J. Nanomed. 16 (2021) 2703–2714.
[31] E. Udofa, Z. Zhao, In situ cellular hitchhiking of nanoparticles for drug delivery, Adv. Drug Deliv. Rev. 204 (2024) 115143.
[32] Y. Xia, L. Rao, H. Yao, Z. Wang, P. Ning, X. Chen, Engineering macrophages for cancer immunotherapy and drug delivery, Adv. Mater. 32 (2020) e2002054.
[33] J. Luo, M. Pan, K. Mo, Y. Mao, D. Zou, Emerging role of artificial intelligence in diagnosis, classification and clinical management of glioma, Semin. Cancer Biol. 1 (2023) 110–123.
[34] T. Hollon, C. Jiang, A. Chowdury, M. Nasir-Moin, A. Kondepudi, A. Aabedi, A. Adapa, W. Al-Holou, J. Heth, O. Sagher, P. Lowenstein, M. Castro, L.I. Wadiura, G. Widhalm, V. Neuschmelting, D. Reinecke, N. von Spreckelsen, M.S. Berger, S. L. Hervey-Jumper, J.G. Golfinos, M. Snuderl, S. Camelo-Piragua, C. Freudiger, H. Lee, D.A. Orringer, Artificial-intelligence-based molecular classification of diffuse gliomas using rapid, label-free optical imaging, Nat. Med. 29 (2023) 828–832.
[35] D. Su, Z. Jiang, Y. Xu, J. Li, Q. Qi, Y. Gong, H. Wang, Z. Zhao, X. Zhao, J. Zhou, Molecular design of ternary copolymers with high photothermal performance in the near-infrared window for effective treatment of gliomas in vivo, Acta Biomater. 192 (2025), 302-114.
[36] F. Zeng, Z. Fan, S. Li, L. Li, T. Sun, Y. Qiu, L. Nie, G. Huang, Tumor microenvironment activated photoacoustic-fluorescence bimodal nanoprobe for precise chemo-immunotherapy and immune response tracing of glioblastoma, ACS Nano 17 (2023) 19753–19766.
[37] S. Li, J. Wei, Q. Yao, X. Song, J. Xie, H. Yang, Emerging ultrasmall luminescent nanoprobes for in vivo bioimaging, Chem. Soc. Rev. 52 (2023) 1672–1696.
[38] F.P. García de Arquer, D.V. Talapin, V.I. Klimov, Y. Arakawa, M. Bayer, E. H. Sargent, Semiconductor quantum dots: technological progress and future challenges, Science 373 (2021) eaaz8541.
[39] Q. Xu, J. Gao, S. Wang, Y. Wang, D. Liu, J. Wang, Quantum dots in cell imaging and their safety issues, J. Mater. Chem. B 9 (2021) 5765–5779.
[40] J.C. Kays, A.M. Saeboe, R. Toufanian, D.E. Kurant, A.M. Dennis, Shell-free copper indium sulfide quantum dots induce toxicity in vitro and in vivo, Nano Lett. 20 (2020) 1980–1991.
[41] X. Xie, J. Tang, Y. Xing, Z. Wang, T. Ding, J. Zhang, K. Cai, Intervention of polydopamine assembly and adhesion on nanoscale interfaces: state-of-the-art designs and biomedical applications, Adv. Healthcare Mater. 10 (2021) e2002138.
[42] T. Bedhiafi, S. Idoudi, A.A. Alhams, Q. Fernandes, H. Iqbal, R. Basineni, S. Uddin, S. Dermime, M. Merhi, N. Billa, Applications of polydopaminic nanomaterials in mucosal drug delivery, J. Contr. Release 353 (2023) 842–849.
[43] M. Farokhi, F. Mottaghitalab, M.R. Saeb, S. Thomas, Functionalized theranostic nanocarriers with bio-inspired polydopamine for tumor imaging and chemo-photothermal therapy, J. Contr. Release 309 (2019) 203–219.
[44] I. Mellman, R. Fuchs, A. Helenius, Acidification of the endocytic and exocytic pathways, Annu. Rev. Biochem. 55 (1986) 663–700.
[45] Q. Zheng, T. Lin, H. Wu, L. Guo, P. Ye, Y. Hao, Q. Guo, J. Jiang, F. Fu, G. Chen, Mussel-inspired polydopamine coated mesoporous silica nanoparticles as pH-sensitive nanocarriers for controlled release, Int. J. Pharm. 463 (2014) 22–26.
[46] Q. Chen, Y. Chen, W. Zhang, Q. Huang, M. Hu, D. Peng, C. Peng, L. Wang, W. Chen, Acidity and glutathione dual-responsive polydopamine-coated organic-inorganic hybrid hollow mesoporous silica nanoparticles for controlled drug delivery, ChemMedChem 15 (2020) 1940–1946.
[47] Y.N. Hao, A.Q. Zheng, T.T. Guo, Y. Shu, J.H. Wang, O. Johnson, W. Chen, Glutathione triggered degradation of polydopamine to facilitate controlled drug release for synergic combinational cancer treatment, J. Mater. Chem. B 7 (2019) 6742–6750.
[48] Q. Jiang, M. Pan, J. Hu, J. Sun, L. Fan, Z. Zou, J. Wei, X. Yang, X. Liu, Regulation of redox balance using a biocompatible nanoplatform enhances phototherapy efficacy and suppresses tumor metastasis, Chem. Sci. 12 (2021) 148–157.
[49] P. Yang, F. Zhu, Z. Zhang, Y. Cheng, Z. Wang, Y. Li, Stimuli-responsive polydopamine-based smart materials, Chem. Soc. Rev. 50 (2021) 8319–8343.
[50] X. Chu, L. Zhang, Y. Li, Y. He, Y. Zhang, C. Du, NIR responsive doxorubicin-loaded hollow copper ferrite @ polydopamine for synergistic chemodynamic/photothermal/chemo-therapy, Small 19 (2023) e2205414.
[51] C. Wei, P. Wang, Z. Huang, D. He, W. Zhu, H. Liu, Z. Chen, W. Wang, Y. Li, J. Shen, L. Qin, Construction of surface-modified polydopamine nanoparticles for sequential drug release and combined chemo-photothermal cancer therapy, Mol. Pharm. 18 (2021) 1327–1343.
[52] J. Ruan, H. Liu, B. Chen, F. Wang, W. Wang, Z. Zha, H. Qian, Z. Miao, J. Sun, T. Tian, Y. He, H. Wang, Interfacially engineered Zn_xMn_1-xS@polydopamine hollow nanospheres for glutathione depleting photothermally enhanced chemodynamic therapy, ACS Nano 15 (2021) 11428–11440.
[53] K. Yuki, N. Cheng, M. Nakano, C.J. Kuo, Organoid models of tumor immunology, Trends Immunol. 41 (2020) 652–664.
[54] M. Tang, Q. Xie, R.C. Gimple, Z. Zhong, T. Tam, J. Tian, R.L. Kidwell, Q. Wu, B. C. Prager, Z. Qiu, A. Yu, Z. Zhu, P. Mesci, H. Jing, J. Schimelman, P. Wang, D. Lee, M.H. Lorenzini, D. Dixit, L. Zhao, S. Bhargava, T.E. Miller, X. Wan, J. Tang, B. Sun, B.F. Cravatt, A.R. Muotri, S. Chen, J.N. Rich, Three-dimensional bioprinted glioblastoma microenvironments model cellular dependencies and immune interactions, Cell Res. 30 (2020) 833–853.
[55] R. Mathur, Q. Wang, P.G. Schupp, A. Nikolic, S. Hilz, C. Hong, N.R. Grishanina, D. Kwok, N.O. Stevers, Q. Jin, M.W. Youngblood, L.A. Stasiak, Y. Hou, J. Wang, T. N. Yamaguchi, M. Lafontaine, A. Shai, I.V. Smirnov, D.A. Solomon, S.M. Chang, S. L. Hervey-Jumper, M.S. Berger, J.M. Lupo, H. Okada, J.J. Phillips, P.C. Boutros, M. Gallo, M.C. Oldham, F. Yue, J.F. Costello, Glioblastoma evolution and heterogeneity from a 3D whole-tumor perspective, Cell 187 (2024) 446–463.
[56] S.M. Giannitelli, V. Peluzzi, S. Raniolo, G. Roscilli, M. Trombetta, P. Mozetic, A. Rainer, On-chip recapitulation of the tumor microenvironment: a decade of progress, Biomaterials 306 (2024) 122482.
[57] D.O. de la Pena, S.M.D. Trabulo, E. Collin, Y. Liu, S. Sharma, M. Tatari, D. Behrens, M. Erkan, R.T. Lawlor, A. Scarpa, C. Heeschen, A. Mata, D. Loessner, Bioengineered 3D models of human pancreatic cancer recapitulate in vivo tumour biology, Nat. Commun. 12 (2021) 5623.
[58] D. Dhamecha, D. Le, T. Chakravarty, K. Perera, A. Dutta, J.U. Menon, Fabrication of PNIPAm-based thermoresponsive hydrogel microwell arrays for tumor spheroid formation, Mater. Sci. Eng. C 125 (2021) 112100.
[59] H.H. Gustafson, D. Holt-Casper, D.W. Grainger, H. Ghandehari, Nanoparticle uptake: the phagocyte problem, Nano Today 10 (2015) 487–510.
[60] C. Zhang, J. Tang, W. Xie, F.M. Allioux, Z. Cao, J.M. Biazik, M. Tajik, F. Deng, Y. Li, R. Abbasi, M. Baharfar, M. Mousavi, D. Esrafilzadeh, K. Kalantar-Zadeh, Mechanistic observation of interactions between macrophages and inorganic particles with different densities, Small 19 (2023) e2204781.
[61] O. Lunov, T. Syrovets, C. Loos, J. Beil, M. Delacher, K. Tron, G.U. Nienhaus, A. Musyanovych, V. Mailander, K. Landfester, T. Simmet, Differential uptake of functionalized polystyrene nanoparticles by human macrophages and a monocytic cell line, ACS Nano 5 (2011) 1657–1669.
[62] S. Ostermann, C. Csajka, T. Buclin, S. Leyvraz, F. Lejeune, L.A. Decosterd, R. Stupp, Plasma and cerebrospinal fluid population pharmacokinetics of temozolomide in malignant glioma patients, Clin. Cancer Res. 10 (2004) 3728–3736.
[63] R. Wang, X. Wang, H. Zhao, N. Li, J. Li, H. Zhang, L. Di, Targeted delivery of hybrid nanovesicles for enhanced brain penetration to achieve synergistic therapy of glioma, J. Contr. Release 365 (2024) 331–347.
[64] Z. Dong, L. Tang, Y. Zhang, X. Ma, Y. Yin, L. Kuang, Q. Fan, B. Wang, X. Hu, T. Yin, Y. Wang, A homing peptide modified neutrophil membrane biomimetic nanoparticles in response to ROS/inflammatory microenvironment for precise targeting treatment of ischemic Stroke, Adv. Funct. Mater. 34 (2024) 2309167.
[65] S. Moon, M. Jung, S. Go, J. Hong, H.S. Sohn, C. Kim, M. Kang, B.J. Lee, J. Kim, J. Lim, B.S. Kim, Engineered nanoparticles for enhanced antitumoral synergy between macrophages and T cells in the tumor microenvironment, Adv. Mater. 36 (2024) e2410340.